CERN/SPSC 2002-002
SPSC/M-674
January 7, 2002

ASACUSA STATUS REPORT

January, 2002

ASACUSA Collaboration

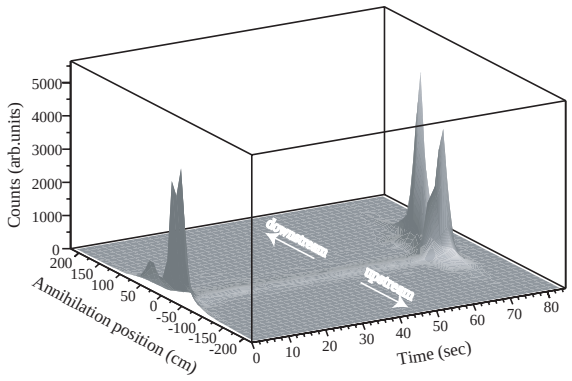

VOLUME 87, NUMBER 9 PHYSICAL REVIEW LETTERS 27 AUGUST 2001

Sub-ppm Laser Spectroscopy of Antiprotonic Helium and a CPT-Violation Limit on the Antiprotonic Charge and Mass

M. Hori,[1] J. Eades,[1] R. S. Hayano,[2] T. Ishikawa,[2] J. Sakaguchi,[2] E. Widmann,[2] H. Yamaguchi,[2] H. A. Torii,[3] B. Juhász,[4] D. Horváth,[5] and T. Yamazaki[6]

[1]*CERN, CH-1211 Geneva 23, Switzerland*
[2]*Department of Physics, University of Tokyo, 7-3-1 Hongo, Bunkyo-ku, Tokyo 113-0033, Japan*
[3]*Institute of Physics, University of Tokyo, Komaba, Meguro-ku, Tokyo 153-8902, Japan*
[4]*Institute of Nuclear Research of the Hungarian Academy of Sciences, H-4001 Debrecen, Hungary*
[5]*KFKI Research Institute for Particle and Nuclear Physics, H-1525 Budapest, Hungary*
[6]*RI Beam Science Laboratory, RIKEN, Wako, Saitama 351-0198, Japan*
(Received 28 March 2001; published 9 August 2001)

Six laser-resonant transitions have been detected in metastable antiprotonic helium atoms produced at the CERN Antiproton Decelerator. They include UV transitions from the last metastable states in the $v = n - \ell - 1 = 0$ and 1 cascades. Zero-density frequencies were obtained from measured pressure shifts with fractional precisions between 1.3×10^{-7} and 1.6×10^{-6}. By comparing these with QED calculations and the antiproton cyclotron frequency, we deduce that the antiproton and proton charges and masses agree to within 6×10^{-8} with a confidence level of 90%.

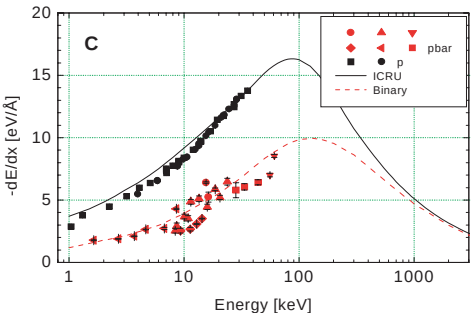

Contents

ASACUSA and its Three Phases **1**

Part 1: ASACUSA Progress during 2001 **2**

1 Experimental Progress in the High-Resolution Spectroscopy of Antiprotonic Helium **3**
1.1 Experimental details . . . 3
1.2 First observation of hyperfine splitting of a $\overline{\mathrm{p}}\mathrm{He}^+$ state using a laser-microwave-laser triple resonance method . . . 4
1.3 Laser spectroscopy of $\overline{\mathrm{p}}\,^4\mathrm{He}^+$ and $\overline{\mathrm{p}}\,^3\mathrm{He}^+$ . . . 9

2 Development of an ultra slow antiproton beam for phase III experiments **16**
2.1 Trapping and Cooling . . . 16
2.2 Extraction . . . 19

3 Experimental Progress in Determining the Energy Loss of Slow Antiprotons **21**
3.1 May 2001 run. . . . 21
3.2 Experimental results . . . 22
3.3 Conclusion : . . . 23

Part 2: ASACUSA Plans for 2002 **25**

4 $\overline{\mathrm{p}}\mathrm{He}^+$ Spectroscopy **26**

5 Ionization in Collisions of Slow Antiprotons and Atoms **27**
5.1 Ionization . . . 27
5.2 Experimental apparatus. . . . 28
5.3 Status . . . 29

6 Antiprotonic atom production **29**
6.1 Formation process calculations for protonium . . . 30
6.2 Metastability in multielectron antiprotonic atoms . . . 31
6.3 Practical realisations - the ASACUSA gas-jet target . . . 31

Part 3: 2003 and beyond **33**

7 Sub-ppb Laser Spectroscopy of Antiprotonic Helium **33**

8 Ionization of Atoms: Kinematically Complete Experiments **33**
8.1 Mid-term running plan: Status of preparation . . . 36
8.2 Long-term perspectives: Multiple ionization using an electrostatic storage ring. . . . 36
8.3 Table top $\bar{p}$ storage ring . . . 37

9 Measurement of protonium and other X-ray spectra **39**
9.1 A Possibility of Protonium X-ray Spectroscopy at the AD . . . 39
9.2 Antiprotonic X-rays from selected isotopically separated targets . . . 42

ASACUSA and its Three Phases

In October 1997 we presented our proposal CERN SPSC/ 97-19, SPSC P-307 to the SPS Committee[1], in which we outlined our plans for a series of AD experiments on "Atomic Spectroscopy And Collisions Using Slow Antiprotons" (ASACUSA), evolving in three phases, each being defined by the nature of the antiproton source, and with frequent switching from one source to another.

Thus the first phase consisted of experiments that could be done with the 5.3 MeV AD beam alone. Second phase experiments required in addition a Radio Frequency Quadrupole Decelerator (RFQD) acting as an AD post-decelerator to reach keV energies, while in the third phase an antiproton trap would be attached to the RFQD to allow experiments with antiproton beams of controlled energy in the eV range. Fig. 1 is the 'roadmap' of the experiment, presented to the SPSC in 1997. Although the start of the whole program had to be delayed by about 1 year, due to the slower-than-expected AD startup, we have very quickly caught up and have now completed more than half of the phase 1 program, nearly 1/2 of the phase 2 program, and almost finished the commissioning of the phase 3 infrastructure.

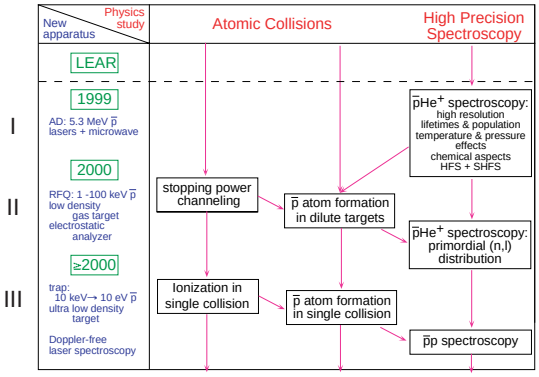

Figure 1: *The three phases of ASACUSA experiments, as presented at the SPSC meeting in November 1997.*

Since the summer of 2000, when AD 'physics' run was started, our phase 1 programme of experiments on the high-precision spectroscopy of antiprotonic helium atoms ($\overline{\mathrm{p}}\mathrm{He}^+$) has consistently been producing new results, one of which, a "CPT test of antiproton mass and charge to 60 ppb precision", has recently been published in Physical Review Letters[2]. Data for 2001 will probably improve this precision still further. This has now (August 2001) been followed by a successful 'laser-microwave triple resonance' experiment, which revealed the hyperfine structure of $\overline{\mathrm{p}}\mathrm{He}^+$, and should make it possible to determine the $\overline{\mathrm{p}}$ magnetic moment with high precision. Furthermore, in 2001, several new transitions were found in both ^{3}He and ^{4}He, and further studies have been made of some already known ones.

In the meantime the (phase 2) RFQD has been constructed, tested, and installed in the AD hall. Within weeks of the installation, in November 2000, the RFQD beam was used to measure the energy loss of antiprotons down to $\sim$ 10 keV. In May 2001, this was followed up by more measurements, extending the energy region down to $\sim$ 1 keV. These results have been submitted for publication in Physical Review Letters[3]. The RFQD beam was also used in 2001 for laser spectroscopy studies of known $\overline{\mathrm{p}}\mathrm{He}^+$ transitions at extremely low target densities ('dilute targets', fig 1), and a new transition, undetectable at the higher densities of the phase 1 experiments, was found.

Finally the phase 3 trap was installed in the spring of 2001, and we succeeded to capture several hundred thousand antiprotons per AD shot by injecting the antiproton beam from the RFQD into it. In October 2001, we successfully cooled down antiprotons in the trap using the electron-cooling technique, and extracted them at an energy of 10 eV.

The present report consists of three parts. In Part 1, we present details of the just-mentioned 2001 achievements. Our plans for 2002 are discussed in Part 2, while in Part 3, we list experiments under discussion within the collaboration.

Part 1: ASACUSA Progress during 2001

Fig. 2 shows how ASASUCA allocated its beamtime to various phases of experiments.

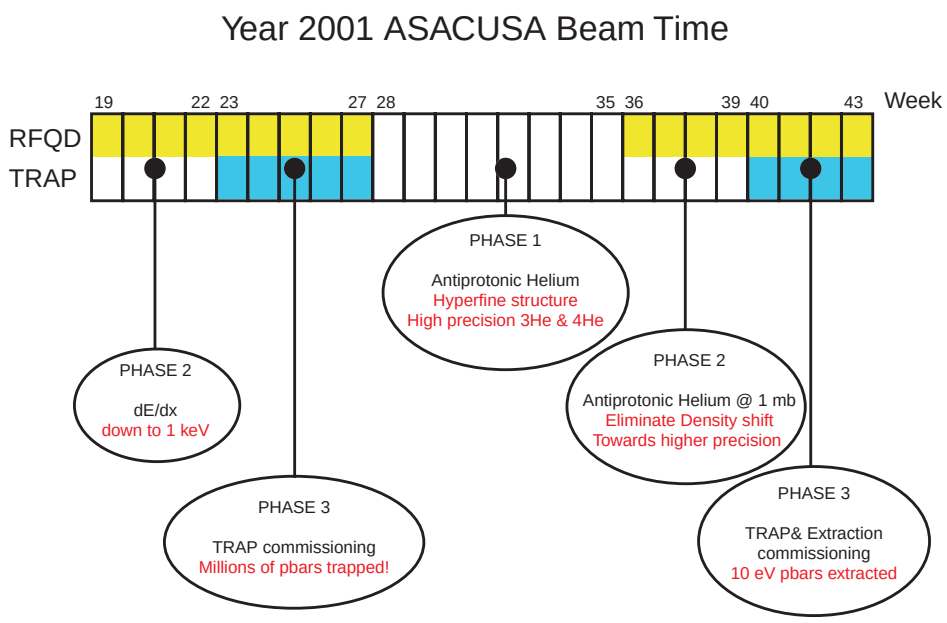

Figure 2: *ASACUSA 2001 beamtime usage.*

Highlights of each of the beam periods are:

Weeks 19-22 The stopping power for antiprotons in various targets were measured in the energy range 1–100 keV using the RFQD. The results have been sent for publication in Physical Review Letters.

Weeks 23-27 Antiprotons were injected from the RFQD into the trap for the first time. We succeeded to trap $\sim 1.5 \times 10^6$ antiprotons per AD shot.

Weeks 28-35 Antiprotonic helium spectroscopy with the phase 1 setup. We succeeded to clearly resolve the $\overline{\mathrm{p}}\mathrm{He}^+$ hyperfine splitting by using the laser-microwave-laser triple-resonance method. This should enable us to set new CPT limits on the $\overline{\mathrm{p}}$ magnetic moment. Our programme of high-precision laser spectroscopy, which had began in 2000 with sub-ppm measurements of four $\overline{\mathrm{p}}\mathrm{He}^+$ transitions, are extended to new transitions in $\overline{\mathrm{p}}\,^4\mathrm{He}^+$ and applied also to $\overline{\mathrm{p}}\,^3\mathrm{He}^+$.

Weeks 36-39 Antiprotonic helium spectroscopy with the phase 2 setup. For the first time, we observed laser resonant transitions in very dilute ($\sim$ 1mb) helium ^{4}He as well as ^{3}He targets, in which collisional shift and broadening can be ignored within the present instrumental resolution. These measurements will make it possible for us to improve the CPT limits of antiprotonic mass and charge. Analyses are in progress.

Weeks 40-43 Trap + ultra low energy beam line commissioning. Antiprotons injected into the trap were cooled by using the electron cooling technique, and were extracted at 10 eV. Although the overall efficiency still needs to be optimized, this marked a great step towards our phase 3 program.

In Section 1, achievements of the $\overline{\mathrm{p}}\mathrm{He}^+$ spectroscopy, both in the phase 1 and phase 2 setups, are described. Section 2 reports on the ultra low energy beam development, and Section 3 describes the antiproton stopping power measurements.

1 Experimental Progress in the High-Resolution Spectroscopy of Antiprotonic Helium

From July to September 2001, we carried out experiments with antiprotonic helium ($\overline{\mathrm{p}}\mathrm{He}^+$) using the direct 5.3 MeV AD beam and the same helium cryogenic target used in 2000. During September we installed the RFQD decelerator in our area ("phase 2"), at the end of which we placed a new, ultra-low density cryogenic target, and succeeded for the first time to observe laser induced transitions on $\overline{\mathrm{p}}\mathrm{He}^+$ at a target pressure about three orders of magnitude lower than we could ever achieve before (sec. 1.3.1).

1.1 Experimental details

1.1.1 Phase 1 setup

In 2001, the AD provided $\sim 4 \times 10^7$ $\overline{\mathrm{p}}$ per shot of $\sim$ 200 ns length with a repetition rate of one shot per two minutes. In phase 1, the antiprotons were stopped in helium gas at temperatures around 6 K and pressures from 0.1 to 2 bar corresponding to number densities of $10^{20} \ldots 10^{21}$ cm^{-3}. As usual, about 3% of the stopped $\overline{\mathrm{p}}$ form metastable $\overline{\mathrm{p}}\mathrm{He}^+$ atoms with average lifetime of ~ 3 μs, and we detected the delayed annihilation products (mostly pions) of antiprotons captured into such atoms with Čerenkov counters viewed by photomultipliers. Their output was gated off during the strong 'flash' corresponding to the uninteresting remainder, the 97% of the antiprotons which annihilate during the AD pulse. The output of the PMTs was directly recorded by a digital oscilloscope as a time-dependent annihilation rate lasting some 20 μs. This constitutes what we refer to as the 'analogue delayed annihilation time spectrum' or ADATS. During this 20μs period, the $\overline{\mathrm{p}}\mathrm{He}^+$ "atomcules" could be irradiated with laser beams and microwave radiation to stimulate transitions of the atom, as we have described in previous reports to this committee.

1.1.2 Phase 2 setup

As described in last year's status report [4], the Radio Frequency Quadrupole Decelerator (RFQD) was built by PS division and tested at the Aarhus tandem, and was first installed in the ASACUSA area at the AD at the end of 2000. It decelerates about 25 % of the antiprotons coming from the AD to energies between 10 and 120 keV. Since it is a very efficient beam transport at 5.3 MeV as well as 100 keV, the un-decelerated portion of the AD beam emerges at the downstream end as well as the decelerated one.

Monte Carlo simulations showed that at the mid-range RFQD output energy ($\sim$ 60 keV), antiprotons could be stopped in helium gas of densities around 10^{17} cm^{-3}. This is about a factor 1000 lower than is required to stop the direct 5.3 MeV AD beam. The bigger stopping volume at this density, and the thinner window needed to transfer keV antiprotons into the gas without too great an energy loss required a cryostat differing radically in design from the one used at 5.3 MeV. As described in the 2000 progress report, a suitable cryostat had already been constructed which could be directly connected to the RFQD vacuum via a 0.9 μm Kapton foil. It could withstand a maximum pressure of a few mbar, our typical operating pressure and temperature being about

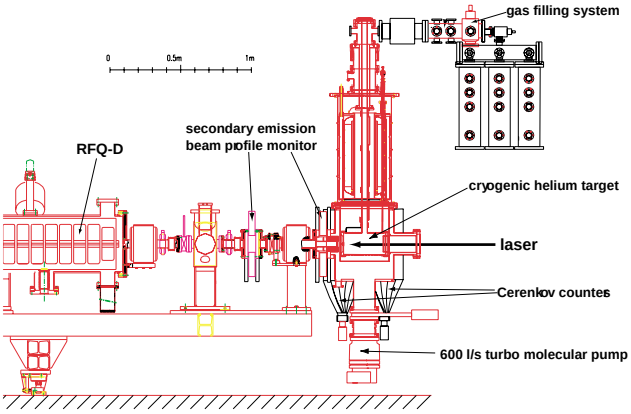

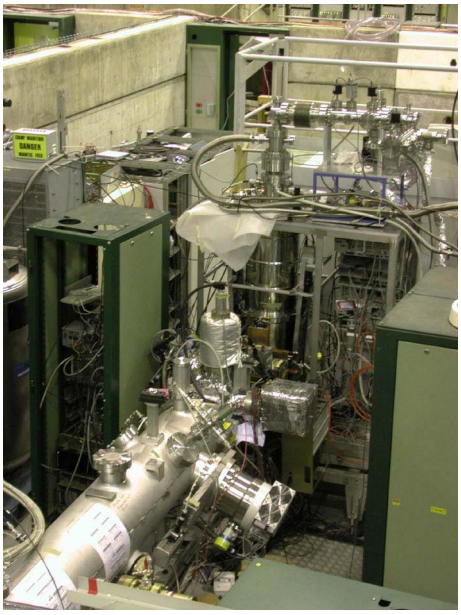

Figure 3: *Left: Drawing of the cryostat built for ultra-low density measurements of* $\overline{\mathrm{p}}He^+$ *attached to the RFQD. Right: picture of the setup in the AD area.*

0.8 mbar and 30 K. Other experimental details of the phase 2 setup (*e.g.* the laser system and the annihilation detectors) were as described for the phase 1 experiments.

1.2 First observation of hyperfine splitting of a $\overline{\mathrm{p}}\mathrm{He}^+$ state using a laser-microwave-laser triple resonance method

In our proposal we described a triple resonance experiment in which a microwave cavity was to be used to measure the spin-flip frequency of the electron in the orbital magnetic field of the antiproton. In this section we report the successful performance of this experiment during August 2001.

1.2.1 Hyperfine structure and laser transitions

The logical followup to the precision measurements of laser transitions of the $\overline{\mathrm{p}}\mathrm{He}^+$ atom (described in section 1.3.1) is the determination of its hyperfine structure. In every atom, energy levels denoted by principal quantum number n and angular momentum quantum number L will be split into sublevels by the magnetic interactions of the constituent particles. The case of metastable antiprotonic helium is unique because of the large angular momentum of the antiproton ($L = 33 \ldots 39$). Therefore, the orbital part will dominate in the expression for the total magnetic moment of the antiproton $\mu(\overline{\mathrm{p}})$,

$$\vec{\mu}(\overline{\mathrm{p}}) = (g_l(\overline{\mathrm{p}})\vec{L} + g_s(\overline{\mathrm{p}})\vec{S_{\overline{\mathrm{p}}}})\mu_{\overline{\mathrm{N}}}, \tag{1}$$

where

$$\mu_{\overline{\mathrm{N}}} = \frac{Q_{\overline{\mathrm{p}}}\hbar}{2M_{\overline{\mathrm{p}}}} \tag{2}$$

is the "anti-nuclear magneton" ($Q_{\overline{\mathrm{p}}}$,$M_{\overline{\mathrm{p}}}$ = charge and mass of the antiproton) and

$$\mu_{\overline{\mathrm{p}}} = \frac{1}{2} g_s(\overline{\mathrm{p}}) \mu_{\overline{\mathrm{N}}}. \tag{3}$$

is the spin magnetic moment of the antiproton. Evidently the mutual interactions between the two spins and the orbital moment, will split each state (n, L) into a quadruplet. However, as the electron's spin moment is much larger than the antiproton's, the dominant level splitting arises from the interaction of the antiproton angular momentum with the electron spin. Let us then write the spin coupling scheme as:

$$\vec{F} = \vec{L_{\overline{p}}} + \vec{S_e} \tag{4}$$

$$\vec{J} = \vec{F} + \vec{S_{\overline{p}}} = \vec{L_{\overline{p}}} + \vec{S_e} + \vec{S_{\overline{p}}}. \tag{5}$$

Since the two particles involved are not the of the same kind we refer to the coupling of eq. 4) as a *hyperfine* structure effect (HFS), in keeping with the familiar hydrogen atom terminology. The interaction of the much smaller antiproton spin with the electron one will then split each member of the resulting doublet into a finer doublet according to the spin coupling of (eq. 5). Its spacing being much smaller than that of the HFS, we refer to this splitting as a *superhyperfine* structure (SHFS) effect.

The fourfold splitting of metastable states has been calculated by Bakalov and Korobov [5]. In general, the HFS is of order $10 \ldots 15$ GHz, while the SHFS is about two orders of magnitude smaller ($100 \ldots 300$ MHz).

According to these calculations, HFS splittings for adjacent states in constant-v chains ($v \equiv n - L_{\bar{p}} - 1$ being the vibrational quantum number) are almost the same. Transitions along these chains are 'favoured' by large transition dipole moments and are easier to detect. Those which change v are 'unfavoured' in the sense that they have smaller dipole moments and therefore weaker line intensity. Their magnetic splittings are however larger and easier to measure (as can be seen

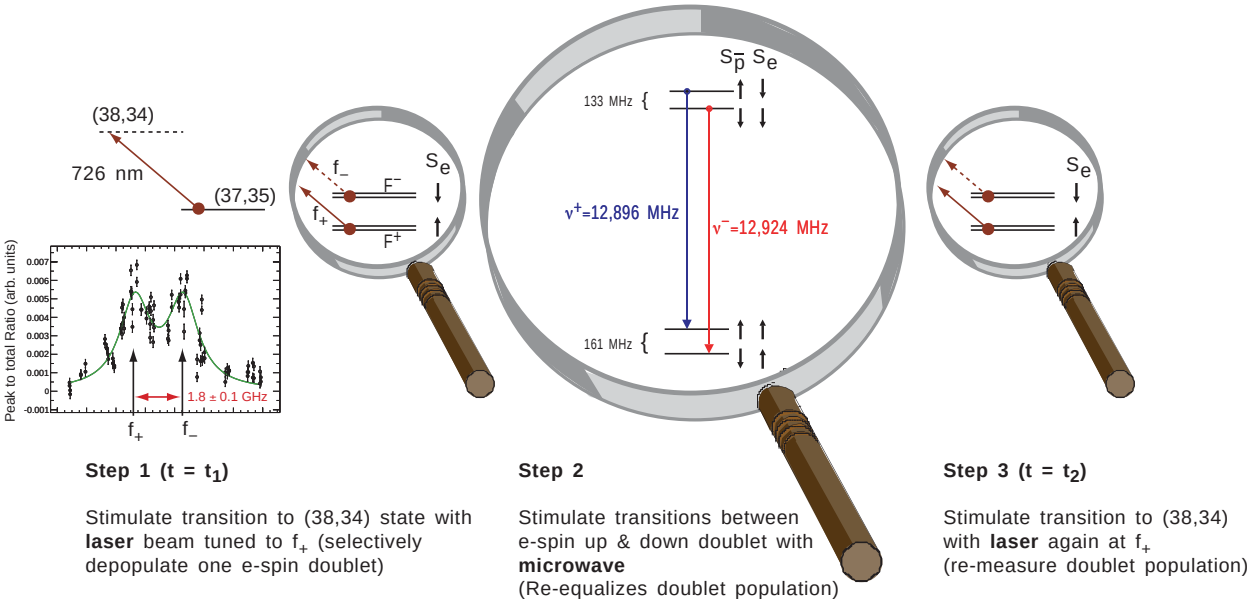

Figure 4: Principle of the laser-microwave-laser triple resonance spectroscopy.

from fig. 4 below). Already at LEAR therefore we scanned the unfavoured $\Delta v = 2$, $(n, L_{\bar{p}}) = (37, 35) \rightarrow (38, 34)$ transition at 726.1 MHz with the best available resolution of our laser system, observing a doublet structure originating from the different HFS splittings of the (37,35) and (38,34) states. Fig. 4 (left) shows the corresponding high resolution scan performed at the AD. The two peaks correspond to non-electron-spinflip transitions between (37,35) and (38,34), the finer SHFS structure being much too small to be resolved. The observed splitting of $\Delta\nu_{\mathrm{HF}} = 1.8 \pm 0.1$ GHz agrees well with the theoretical value of 1.77 GHz [5].

1.2.2 Laser-microwave-laser triple resonance method

Due to the limited resolution of our pulsed laser system (bandwidth ~ 600 MHz) and the Doppler broadening of ~ 400 MHz, the achievable precision on $\Delta\nu_{\mathrm{HF}}$ is rather limited. Furthermore, as it only measures the *difference* of the HFS of two states, the information it contains is incomplete. In order to measure the splitting of a single state, one has to induce direct microwave transitions between the upper and lower pairs of the quadruplet. This can only be done if a population difference is first created between the upper and lower doublets, which were, to begin with, equally populated by the production process. As outlined in our proposal [1] and depicted in Figure 4, we devised a laser-microwave-laser triple resonance method for this purpose. First, a laser pulse tuned to one of the doublet lines (e.g. $f = f_+$ (cf. Fig. 4) selectively depopulates the lower HF doublet

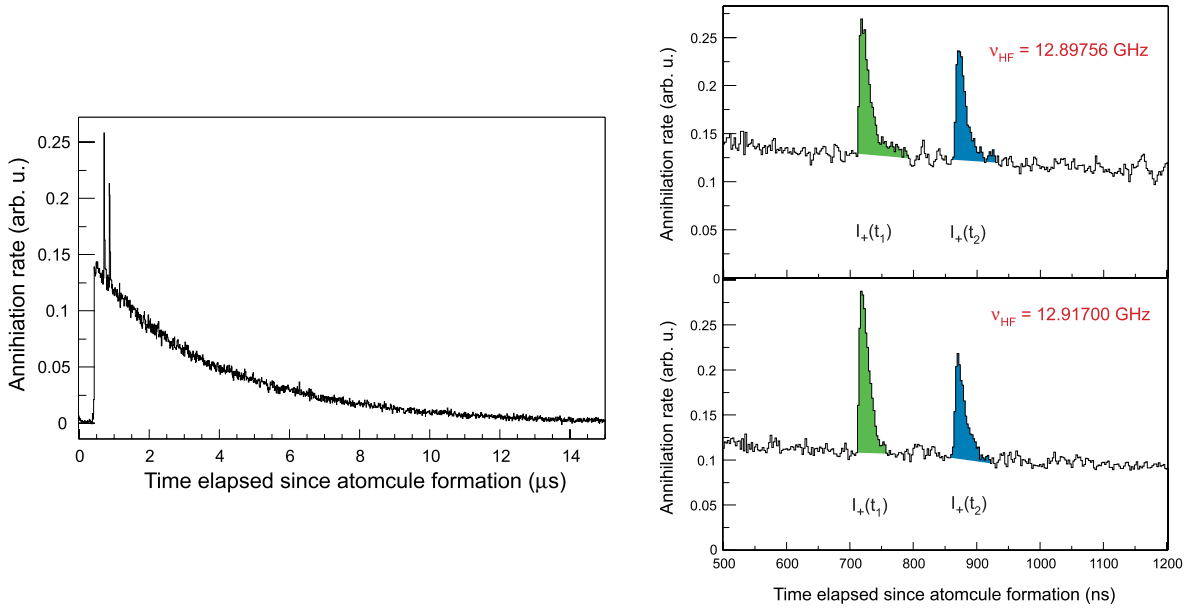

Figure 5: Left: Full ADATS with two successively fired laser pulses at 726.1 nm. The steep rise at $t \sim 500$ ns after the center of the AD pulse is due to the end of the gating pulse that suppresses the PMT output during the AD pulse. Right: Expanded view around the laser pulses of two ADATS, one where additional microwave radiation was applied on resonance (upper), and one off resonance (lower) (the 'off-resonance' is really between the two microwave peaks shown in figure 5). The coloured areas correspond to the resonance intensities I_+. The on-resonance figure clearly shows a larger ratio $I_+(t_2)/I_+(t_1)$ than the off-resonance one. But for the two ADATS $I_+(t_1)$ is different, indicating that the shot-by-shot fluctuations of the resonance intensities are comparable to the expected signal. An averaging over many AD shots is therefore necessary to obtain a statistically significant result.

$F^+ = L_{\bar{p}} + 1/2$ at time t_1, thereby superimposing a spike of intensity $I_+(t_1)$ on the ADATS . On-resonance microwave radiation (i.e. $\nu = \nu^+_{\rm HF}$ or $\nu = \nu^-_{\rm HF}$) is then applied until t_2, and partially re-equalizes the populations of the F^+ and F^- doublets. Finally, a second laser pulse with $f = f_+$ at $t = t_2$ probes the population of the F^+-levels at t_2, producing a second ADATS spike of intensity $I_+(t_2)$.

The quantity to be measured is therefore the intensity ratio

$$R^{++}(\nu_{\rm HF}) \equiv \frac{I_+(t_2)}{I_+(t_1)} \tag{6}$$

as a function of microwave frequency. Fig. 5 shows examples of ADATS with two successively applied laser pulses of 726.1 nm wavelength, for cases when the microwave source was tuned on and off an expected resonant value. The second laser pulse was generated by splitting part of the beam and making multiple reflections between mirrors to generate a time delay $\Delta t = t_2 - t_1$. Practical problems of beam alignment limited the achievable separation to to 150 ns, which gives a frequency resolution of the experiment of $\Delta\nu = 1/(2\pi\Delta t) = 1.1$ MHz. A clear difference in the intensity ratio R^{++} can be seen for the two examples of Fig. 5 (right). The reason why a second peak is still present in the off-resonance case is that the first laser does not fully depopulate the state completely (some spontaneous feeding of the quadruplet from higher states can also occur during the interval $t_2 - t_1$).

1.2.3 Result and comparison to theory

Fig. 6 (left) shows the preliminary result of a scan over a range of microwave frequencies around the predicted values for the $(37, 35)$ state. Clearly two resonances are observed around the $\nu^+_{\rm HF} = 12.896$ GHz and $\nu^-_{\rm HF} = 12.924$ GHz. During this year's beam time we were able to perform in total five scans of the HF structure, each lasting one AD shift including the necessary preparations, and

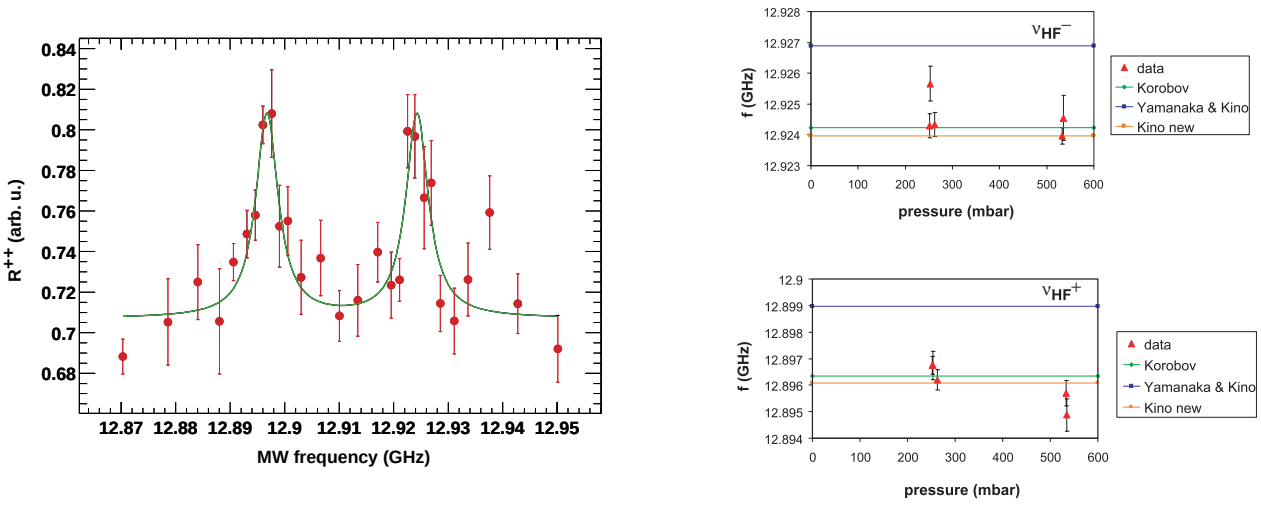

Figure 6: PRELIMINARY RESULTS OF ONLINE ANALYSIS. Left: Intensity ratio R^{++} (cf. eq. 6) as a function of microwave frequency. The points show the data obtained during one AD shift of 8 hours corresponding to ~ 180 AD shots. Two resonances can be clearly seen around the theoretically predicted frequencies. The curve shows the result of a fit of two Lorentz curves. Right: Comparison of the results of the fits for $\nu^+_{\rm HF}$ and $\nu^-_{\rm HF}$ with theory. Each data point corresponds to data taken during one AD shift. We took data at two pressures of the helium gas.

containing about 200 AD shots. The resulting experimental values for $\nu^+_{\rm HF}$ and $\nu^-_{\rm HF}$ are compared in Fig. 6 (right) to the most up-to-date theoretical values listed in Table 1. These consist of an improved calculation by Bakalov and Korobov [6] and an independent evaluation by Yamanaka, Kino et al. [7]. The latter authors used the same Hamiltonian, but a different numerical method, and have recently improved their calculation of the HF splitting [8]. It is remarkable that all theoretical values agree with the experiment on the level of $\sim 2\times10^{-4}$, and the most recent values of both groups ([6] and [8], resp.) at a level of $< 3\times10^{-5}$. This corresponds roughly to the current accuracy of both calculations which is limited by the omission of terms of relative order $\alpha^2 \approx 5\times10^{-5}$.

In our preliminary analysis, the error bars for the frequencies are of the order of $0.4\ldots0.7$ MHz, corresponding to a relative accuracy of $3\ldots5\times10^{-5}$. The width of the lines is about $4\ldots8$ MHz, so that the center is determined to about a factor 10 better. This might be improved if the offline analysis reduces the fluctuations of the data points. The width of the lines is larger than our intrinsic resolution of ~ 1 MHz indicating that other sources (collisional broadening, residual static magnetic field, etc.) are the main contributors to the line width. A theoretical estimation of Korenman [9] concluded that the shift of the HF lines is very small (about 12 kHz or 10^{-6} relative at our density of 3×10^{20} cm^{-3}), while the broadening will be ~ 2 MHz. Under this assumption we can average all the data points and obtain:

$$\begin{aligned}\nu^+_{\rm HF} &= 12.89624 \pm 0.00019\text{GHz}\\ \nu^-_{\rm HF} &= 12.92430 \pm 0.00018\text{GHz (all values preliminary).}\end{aligned}$$

transition	Korobov and Bakalov [6]	Yamanaka and Kino [7]	Kino (new values) [10]
$\nu_{\rm HF}$	12.906 0110	12.908 648	12.905 73495
$\nu^+_{\rm HF}$	12.896 3462	12.898 977	12.896 07391
$\nu^-_{\rm HF}$	12.924 2428	12.926 884	12.923 96379
$\nu^+_{\rm SHF}$	0.132 9887	0.132 987	0.132 99332
$\nu^-_{\rm SHF}$	0.160 8853	0.160 894	0.160 88320

Table 1: Theoretical values for the HF transitions of the state $(37, 35)$. Many digits are shown, although the accuracy is limited by the omission of higher-order terms of relative $\mathrm{O}(\alpha^2)$ to $\approx 5\times10^{-5}$.

1.2.4 Discussion

The observation of two microwave-induced hyperfine transitions confirm the quadruplet structure of antiprotonic helium as predicted by Bakalov and Korobov [5], with its unique feature of the large splitting caused by the spin-flip of the electron in the orbital magnetic field of the antiproton. The two measured hyperfine frequencies $\nu^+_{\rm HF}$ and $\nu^-_{\rm HF}$ are in excellent agreement with the most up-to date theoretical calculations on the level of the theoretical accuracy of $\approx 5\times10^{-5}$. The averaged experimental precision is $\sim 1\times10^{-5}$, by a factor of 5 better than that of the present theoretical values, calling for a further improvement of the calculations. Since all the calculations assume the QCD properties of the hyperfine structure and also the CPT invariance, we can in turn deduce the spin and orbital magnetic moments of $\bar{\rm p}$.

From the agreement between experiment and theory we can derive a value for the orbital magnetic moment of $\bar{\rm p}$ = $g_l(\bar{p})\ \mu_{\overline{\rm N}}$, namely, orbital g-factor $\times$ antinuclear magneton. What is

noteworthy is that no such experimental value exists for the proton, atoms with an orbiting proton being unavailable. The corresponding g-factor ($g_l(p)$) is always therefore *assumed* to be identically equal to one together with a *defined* nuclear magneton. For the antiproton, we can derive an experimental limit from our measurements of $\nu^+_{\rm HF}$ and $\nu^-_{\rm HF}$:

$$|g_l(\overline{p}) - 1| \leq 5 \times 10^{-5}, \tag{7}$$

where the upper limit is constrained by the present theoretical accuracies for $\nu^+_{\rm HF}$ and $\nu^-_{\rm HF}$ whereas the experimental precision is 1×10^{-5}. This is the first measurement of an orbital g-factor for either particle.

The observed microwave transitions $\nu^+_{\rm HF}$ and $\nu^-_{\rm HF}$ yield values for the spin magnetic moment of the antiproton in a less sensitive way because they depend on the difference of the SHF splittings of the F^+ and F^- sublevels. Bakalov [11] calculated a sensitivity factor of $\delta\nu/\delta\mu_{\overline{\rm p}} = 0.0065$ GHz$/\mu_{\rm N}$ for the $\nu^+_{\rm HF}$ transition. The current precision of $\Delta\nu_{exp} = 1.5 \times 10^{-5}$ therefore results in an error for the spin magnetic moment of the antiproton of

$$\Delta\mu^{exp}_{\overline{\rm p}} = \frac{\Delta\nu_{exp}}{\delta\nu/\delta\mu_{\overline{\rm p}}} = \frac{1.9 \times 10^{-4}\ \text{GHz}}{0.0065\ \text{GHz}/\mu_{\rm N}} = 0.03\ \mu_{\rm N}. \tag{8}$$

The current best limit on $\Delta\mu^{exp}_{\overline{\rm p}}$ comes from a spin-orbit splitting measurement in antiprotonic lead atom, $\mu_{\overline{\rm p}} = 2.800 \pm 0.008\ \mu_{\rm N}$ [12], which is four times better than that of our preliminary value.

By reducing the linewidth and improving our statistics, we may be able to make our own limit competitive with the X-ray value. Any value derived for $\mu_{\overline{\rm p}}$ from the $\overline{\rm p}{\rm He}^+$ atom will nevertheless remain an indirect estimate unless we can measure antiproton spin-flip transitions at ~ 150 MHz directly.

1.3 Laser spectroscopy of $\overline{\rm p}\,^4{\rm He}^+$ and $\overline{\rm p}\,^3{\rm He}^+$

In 2001 we continued our laser spectroscopic studies of $\overline{\rm p}\,^4{\rm He}^+$ and $\overline{\rm p}\,^3{\rm He}^+$ both with the 5.3 MeV AD beam and with a 60 keV beam from the RFQD.

In the direct AD beam case the $\overline{\rm p}$ beam was stopped in the cryostat already used in 2000 for these investigations. This contained gas at 6.1K and 0.1-0.2 bar. In $\overline{\rm p}\,^4{\rm He}^+$, We found four new 'unfavoured' transitions, characterised by a change $\Delta v = 2$ in the vibrational quantum number $v \equiv n - l - 1$. As stated above, these are so called because they have a smaller dipole moment than the $\Delta v = 0$, 'favoured' transitions, and are therefore more difficult to find. Fig. 7 (upper) shows all transitions in $\overline{\rm p}\,^4{\rm He}^+$ observed to date. In $\overline{\rm p}\,^3{\rm He}^+$ we found five new transitions and made a detailed study of the density dependence of their transition energies. The same density dependence was also investigated for three transitions previously seen at LEAR, for which no such studies had been made. Fig. 7 (lower) shows the current situation for $\overline{\rm p}\,^3{\rm He}^+$. These shifts are of importance for CPT tests and for obtaining a full picture of parent state lifetimes and populations, and the Auger lifetimes of the daughter states.

In the RFQD beam experiments we used the new cryostat to investigate the important regime in which the $\overline{\rm p}{\rm He}^+$ atom undergoes relatively few collisions during its microsecond lifetime. With helium gas density one thousand times lower than is needed to stop the direct 5.3 MeV AD beam, we were able to reproduce in this regime many previously seen transitions, and detected for the first time the last transition in the outermost ($v = 0$) cascade $(n, l) = (32, 31) \rightarrow (31, 30)$ at $\lambda = 264.7$ nm, since at the higher densities previously available, this transition was invisible owing to collisional quenching.

The following sections describe these results and the conclusions that can be drawn from them.

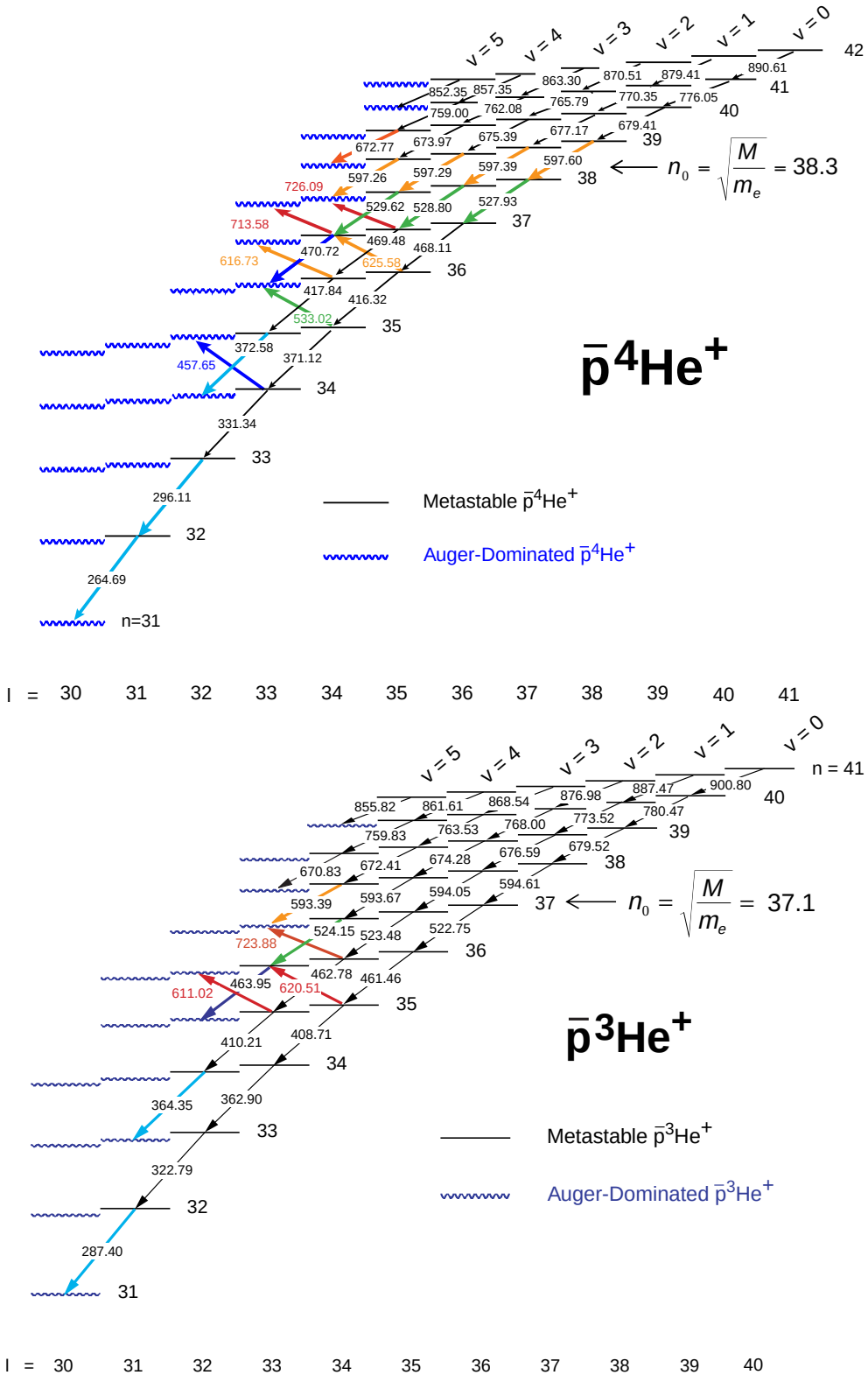

Figure 7: *Energy level diagrams of* $\overline{\mathrm{p}}\,^4He^+$ *(upper) and* $\overline{\mathrm{p}}\,^3He^+$ *(lower). Observed transitions are denoted by bold arrows. Their wavelengths are indicated in nm.*

1.3.1 *Determination of density shift and zero-density transition wavelengths: CPT test for the antiproton charge and mass*

The precise measurement of the density dependence of transition energies makes possible their extrapolation to zero density. The zero-density values can then be compared to three-body QED calculations. As explained in the status report for 2000 [4], we could achieve in $\overline{\mathrm{p}}\,^4\mathrm{He}^+$ an experimental accuracy of 1.3×10^{-7} in the best case [2], and the most sophisticated three body calculations [13, 14] agreed with the experimental values within $(\nu_{\mathrm{th}}-\nu_{\mathrm{exp}})/\nu_{\mathrm{exp}} \leq 5\times10^{-7}$ for transitions with natural linewidths < 50 MHz. Since the theorists use the better known numerical values for the proton mass M_{p} and charge Q_{p} in their calculations, the agreement theory-experiment can be used to set a limit on the equality of proton and antiproton charge and mass. With last year's measurement of four transitions in $\overline{\mathrm{p}}\,^4\mathrm{He}^+$ we could set a new limit of $(M_{\mathrm{p}}-M_{\overline{\mathrm{p}}})/M_{\mathrm{p}} = (Q_{\mathrm{p}}+Q_{\overline{\mathrm{p}}})/Q_{\mathrm{p}} < 6\times10^{-8}$, a factor 8 better than our previous value from LEAR [15] and a factor 300 more precise the old values obtained from X-ray spectroscopy of antiprotonic atoms [12, 16]. This result was published as the first PRL paper from the AD [2].

In 2001 we could measure the density shift for three more transitions in $\overline{\mathrm{p}}\,^4\mathrm{He}^+$, and five in $\overline{\mathrm{p}}\,^3\mathrm{He}^+$. The data on $\overline{\mathrm{p}}\,^3\mathrm{He}^+$ are of great interest since the isotope effect constitutes a good test for the accuracy of the calculations.

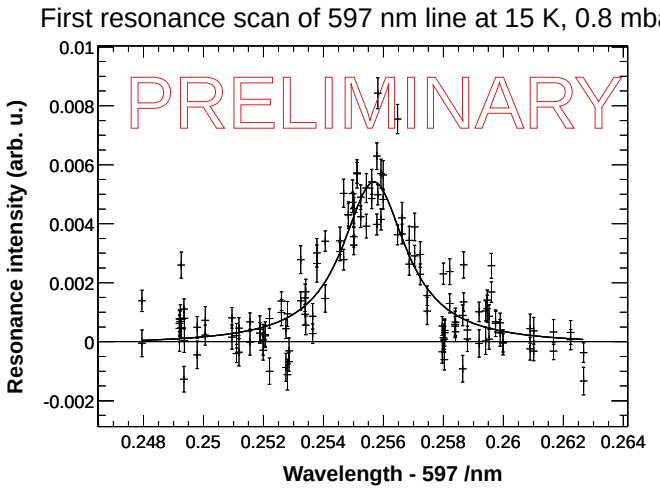

Figure 8: *First resonance scan of the 597 nm line with the RFQD beam.*

In addition, we succeeded to measure the resonance center for most of the observed transitions in both $\overline{\mathrm{p}}\,^4\mathrm{He}^+$and $\overline{\mathrm{p}}\,^3\mathrm{He}^+$ in the ultra-low density target. Fig. 8 shows the first resonance scan of the 597 nm line at 0.8 mbar pressure. This allows to drastically reduce the systematic error coming from the extrapolation to zero density.

Laser spectroscopy using the RFQD beam, however, still needs more refinements (to be done in 2002). Due to the large stopping distribution of antiprotons (extending over $>$ 10 cm) and the background of undecelerated 5.3 MeV antiprotons (they stop in the target walls and create background via the $\pi \rightarrow \mu \rightarrow e$ decay), the resonance intensity was very weak. Due to the low signal intensity the statistical errors of the ultra-low density points are still large. To improve this we plan to install a magnetic spectrometer line after the RFQD that separates the 60 keV beam from the 5.3 MeV component. This should drastically reduce the background from $\pi \rightarrow \mu \rightarrow e$ decay and thus increase the signal-to-noise ratio.

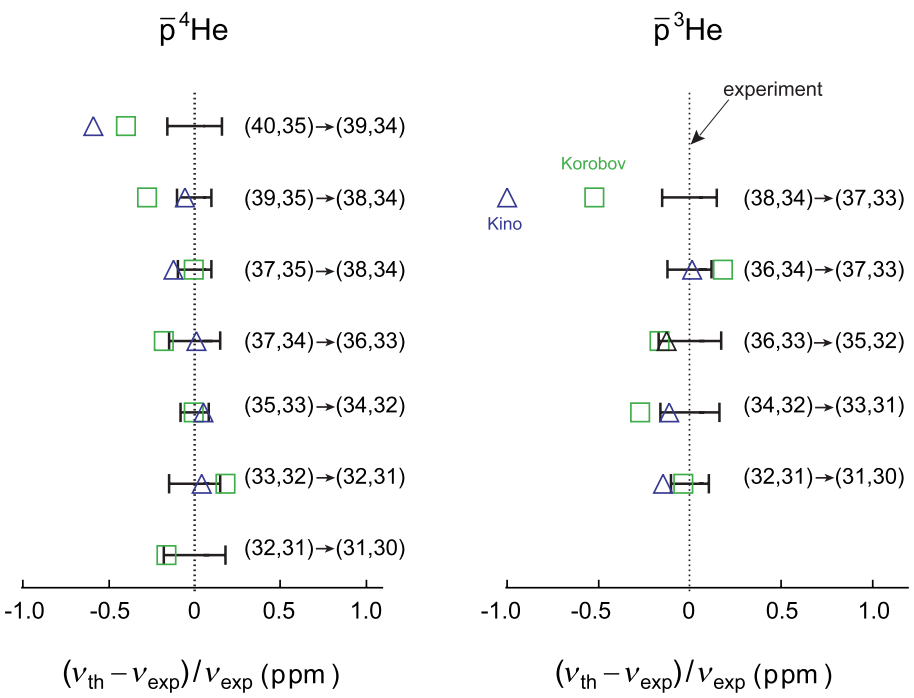

Figure 9: *PRELIMINARY. Relative deviation of zero-density transition frequencies from theoretical calculations by Korobov [13] and Kino [10] for several transitions in* $\overline{\mathrm{p}}\,^4He^+$ *and* $\overline{\mathrm{p}}\,^3He^+$. *The error bars denote the experimental error. In this analysis the results of measurements with the RFQD (section 1.3.1) at ultra-low densities have been included.*

Fig. 9 shows the relative deviations between experimental and theoretical values for all observed transitions to daughter states with natural width < 50 MHz. As explained in the next section, very broad transitions to short-lived daughter states are more difficult to treat theoretically.

Fig. 9 shows again a remarkable agreement on the level of a few 10^{-7} for transitions between lower-lying states. These results already include scans made at ultra-low density with the RFQD. We therefore expect to improve our CPT limit by a factor $2-3$ when the final analysis will be finished. The data also show an almost systematic deviation for higher lying states, which is not yet understood. A possibility is e.g. a larger sensitivity of these states to DC and/or AC Stark shifts, which is currently being investigated.

1.3.2 Auger decay rates of $\overline{\mathrm{p}}He^+$ *states*

Apart from external influences, the total lifetime of a state of $\overline{\mathrm{p}}\mathrm{He}^+$ is determined by its radiative (τ_r) and Auger (τ_A) lifetimes. The Auger lifetimes depend strongly on the *transition multipolarity* L, which is the angular momentum carried away by the electron [17]. Typically the Auger rate ($\lambda_A \equiv 1/\tau_\mathrm{A}$) is of the order of

$$\lambda_A \sim 10^{17-3L}\ \mathrm{s}^{-1} \text{ for } L = 2, 3, 4. \tag{9}$$

Since the radiative decay rates of the states are about $10^5 - 10^6$ s^{-1}, a state is no more metastable (i.e. "short-lived") when the possible minimum $L \equiv L_0$ satisfies $L_0 \leq 3$. In a laser transition, the lifetime of the Auger-dominated short lived state determines the intrinsic (natural) width Γ via the

relation $\Gamma = 1/(2\pi\tau_{\rm A})$. Typically, the width of a transition to a level with $L = 3$ is $\Gamma \sim 10$ MHz, to one with $L = 2$ it is $\Gamma \sim 10$ GHz. The latter is much larger than our experimental resonance line width of $\sim 1 - 5$ GHz.

Fig. 10 gives an overview on experimental and theoretical Auger rates as determined from data taken in 2000. We found two surprising properties among the newly discovered transitions:

1. the resonance $(n, l) = (36, 34) \rightarrow (37, 33)$ had a width of ~ 20 GHz in spite of its daughter state having multipolarity $L = 3$. Furthermore, the zero-density wavelength deviated from the theoretical value of Korobov [13] by ~ 80 ppm.

2. the last transition in the outermost cascade with $v = 0$ was found to be the $(n, l) = (33, 32) \rightarrow (32, 31)$. This means the lifetime of the $(32, 31)$ state is ns or shorter in spite of n its daughter state having multipolarity $L = 4$ ($\lambda_A \sim 10\mu s^{-1}$, see Eq. 9).

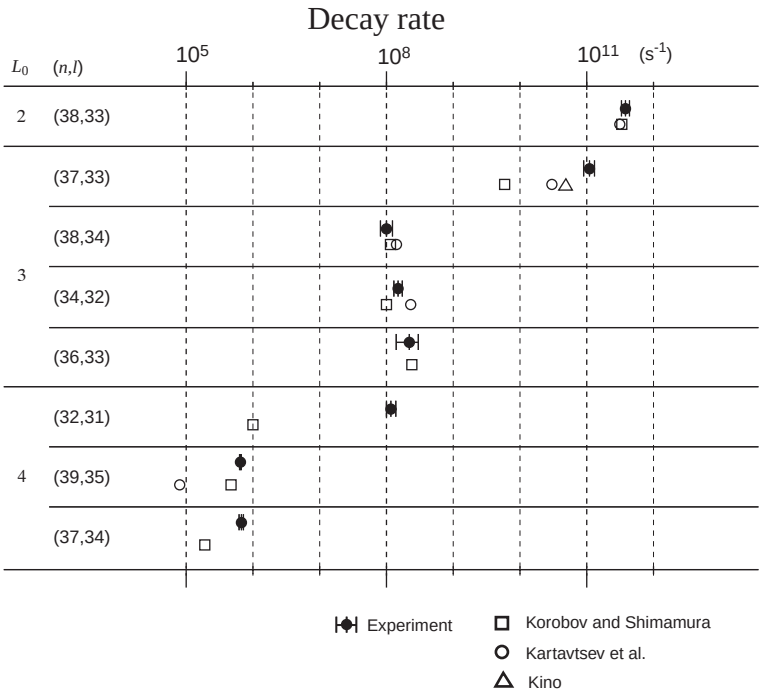

Figure 10: *Decay rate comparison in log scale. Experimental values and results of three different calculations of Auger decay rates are shown (□ from [18], ◯ from [19], △ from [10]). L_0 is the minimum transition multipolarity of Auger decay. The indicated numbers 10^{11} s^{-1}, 10^8 s^{-1} and 10^5 s^{-1} are the typical values for the transition multipolarity $L = 2, 3, 4$, respectively.*

A possible explanation had been given by Kartavtsev et al. [19] already before our experiment took place. They investigated the influence of states where the electron is not in it's ground state, but in an excited orbital. Such states are very short lived, and had therefore not been considered in connection with the metastable states. Kartavtsev et al. pointed out that there will be a configuration mixing effect between metastable states and states with excited electron configurations, provided *i)* they lie energetically close and *ii)* they have the same *total* angular momentum. In the case of the $(37, 33)$ state, there is a $l = 33$ state with the configuration $(32, 31)_{\bar{p}} \otimes (3d)_e$ close by, where the electron is in a 3d state. The admixture of this "excited electron" state shortens the lifetime of the $(37, 33)$, which causes the unexpected large width of this state.

Kartavtsev et al. offered the same explanation for the $(32, 31)$ state, but both Korobov and Kino failed to find a close-lying "excited electron" state with their more sophisticated calculations. In 2001 we could observe the lower transition $(n, l) = (32, 31) \rightarrow (31, 30)$ in measurements with the RFQD and the low-density target cryostat, at a density of 3×10^{17} cm^{-3}, three orders of magnitude lower than we used in 2000. This shows that the shortening of the $(32, 31)$ lifetime was caused by collisional quenching, not by configuration mixing.

Configuration mixing not only changes the lifetime, but it also affects the state energy and therefore the wavelength of a laser transition to this state. The observed width of $\Gamma \sim 20$ GHz corresponds to ~ 40 ppm. Surprisingly, the theoretical value of Kino [10] deviates only a few ppm from the experimental one [2], while Korobov's value [20] is about 80 ppm away. The results presented here are almost ready for publication in Phys. Rev. A.

1.3.3 Determination of initial populations

The intensity $I(t_{\mathrm{L}})$ of a laser-induced transition is directly proportional to the population of the parent state $P_{(n,l)}(t_{\mathrm{L}})$ at the time t_{L} of the arrival of the laser pulse. By measuring $I(t_{\mathrm{L}})$ for various settings of t_{L}, the time evolution of the state population can be mapped out, and extrapolation to time zero allows the determination of the initial population $P_{(n,l)}(0)$ for any parent state of a transition.

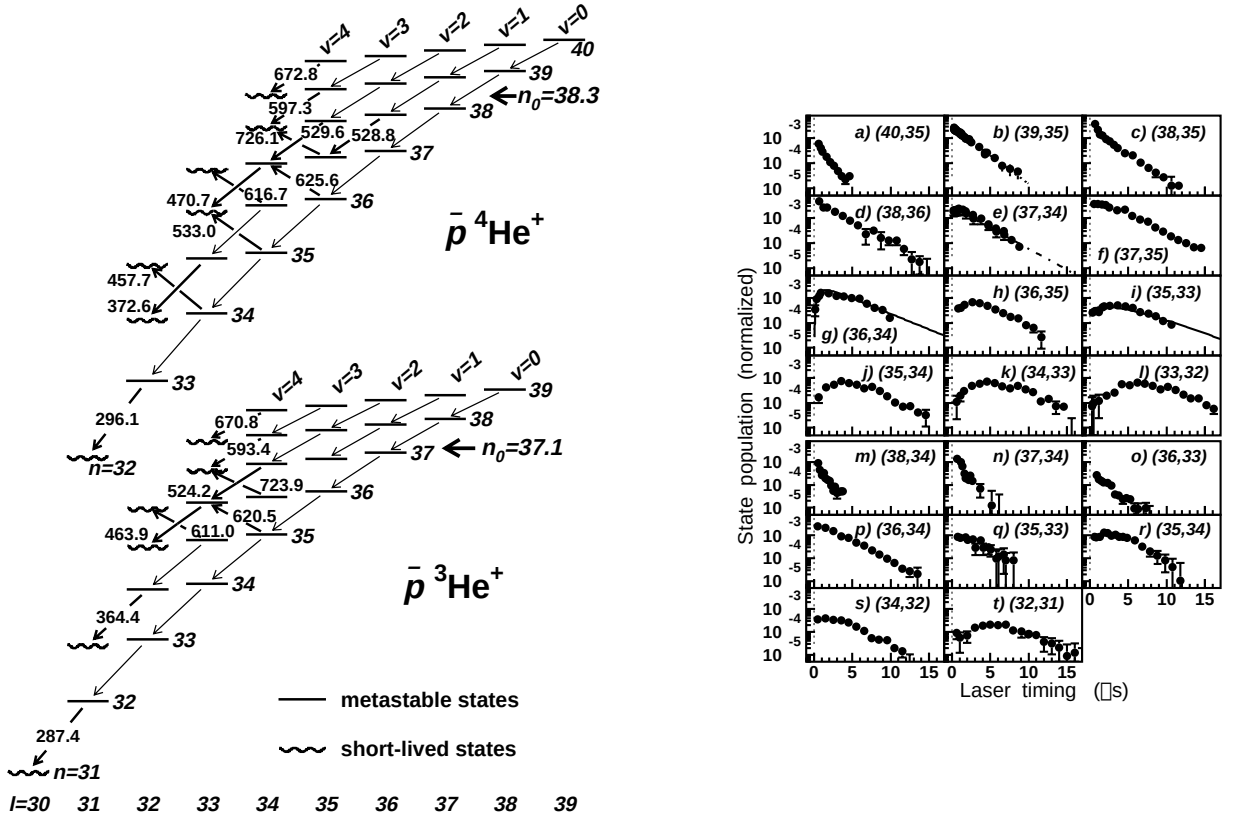

Figure 11: *Left: Energy level diagrams of* $\overline{\mathrm{p}}\,^4He^+$ *and* $\overline{\mathrm{p}}\,^3He^+$. *The wavelengths of some of the observed transitions are indicated in nm. The 670.8 nm transitions in* $\overline{\mathrm{p}}\,^3He^+$ *was searched for but not found. Right: Time evolutions of the populations in twelve* $\overline{\mathrm{p}}\,^4He^+$ *(a–l) and eight* $\overline{\mathrm{p}}\,^3He^+$ *(m–t) states. The best fit of a cascade model is shown by solid lines.*

The large number of observed transitions (cf. Fig. 11) enables us to determine the initial population of nearly all metastable states in both $\overline{\mathrm{p}}\,^4\mathrm{He}^+$ and $\overline{\mathrm{p}}\,^3\mathrm{He}^+$, and thus the total metastable fraction. It turns out that in $\overline{\mathrm{p}}\,^4\mathrm{He}^+$, the region $n = 37 - 40$ accounts for nearly all of the observed $(3.0 \pm 0.1)\%$ fraction of antiprotons captured into metastable states. In $\overline{\mathrm{p}}\,^3\mathrm{He}^+$ atoms the antiprotons are distributed over the region $n = 34-38$, which accounts for the observed $(2.4\pm0.1)\%$ metastability. Thus for the first time we have been able to locate all the antiprotons captured into metastable states.

This and the fact that no significant population was found above $n = 40$ in $\overline{\mathrm{p}}\,^4\mathrm{He}^+$ is in sharp contrast to most of theoretical calculations [21, 22, 23], who predict total trapping fractions of $20 - 30\%$, and initial capture of antiprotons up to $n = 50$ and above. There exist two explanations for this discrepancy:

- Korenman [21] suggests that $\overline{\mathrm{p}}\mathrm{He}^+$ atoms created in the $n \geq 41$ states recoil with such large kinetic energies that they are rapidly destroyed by collisions during the thermalization process.
- Sauge and Valiron [24] predict that the quenching cross sections for the $n \geq 41$ states are large even at thermal velocities.

An experimental verification might be possible in ultra-low density experiments using the RFQD beam (see next section), when the $\overline{\mathrm{p}}$ thermalization times get long enough to be observed.

The results of this subsection have been submitted to Physical Review Letters[25].

2 Development of an ultra slow antiproton beam for phase III experiments

ASACUSA is preparing an ultra-slow monoenergetic antiproton beam by sequentially combining the beams from the AD (down to 5.3MeV), the RFQD (down to several tens keV), and confining them in a multiring electrode trap (MRE) furnished by Tokyo University. Here they are cooled and compressed before being extracted, reaccelerated to eV-scale energies and delivered via a beam transport line to a collision region. The trap and eV-beam transport line are jointly known as "MUSASHI"[1] [26]. The transport region is designed so that a trap pressure more than six orders of magnitude lower than that of the collision region can be maintained, with minimal antiproton loss. MUSASHI will permit collision dynamics to be studied in processes like antiprotonic atom formation and ionization processes under 'single collision conditions' (*i.e.* in which the only atomic collision that takes place is the one being studied). Spectroscopic studies of various metastable antiprotonic atoms such as $\bar{p}p$, $\bar{p}He^{++}$, etc. will also be possible under these conditions.

At least three key techniques, (1) efficient trapping, (2) efficient cooling, and (3) efficient transport of extracted antiprotons are necessary developed to make the MUSASHI project work successfully.

The AD beamtime allocated to the MUSASHI commissioning during the 2001 run amounted to 33 shifts, of which roughly 45% was used for repairs of the PS and tuning of the AD and 15% for tuning the RFQD and the LEBT (the low energy beam transport between the RFQD and the trap) . Only 40% of the time was therefore available for MUSASHI, during which we nevertheless succeeded to trap, cool and extract antiprotons at energies down to 10 eV. However, trapping, cooling and extraction efficiencies need to be further improved in 2002 before MUSASHI can be used for phase 3 experiments.

2.1 Trapping and Cooling

2.1.1 Outline of the methods

Antiprotons decelerated with the RFQD were injected into a multi ring trap (MRT) installed in a 5T superconducting solenoid through a thin degrader foil (two PET foils of $130\mu g/cm^2$) which serves also as a vacuum isolator between the LEBT and the trap. Figure 12 shows the configuration of the degrader foil and the MRT in the solenoid.

After the antiprotons enter the trap through the degrader foil, they continue through the trap towards its downstream end. On reaching the Downstream Catching Electrode (DCE) (see Fig. 12) they are reflected backwards by its negative bias towards the Upstream Catching Electrode (UCE). A -10 kV bias applied to this during the meantime ensures that they remain confined within the MRT.

The elements of the multi-ring structure are biased so as to generate a harmonic potential within a volume large enough [27, 28] (radius ~ 1 mm, length ~ 50 mm) to store more than 10^7 antiprotons as well as some 10^9 electrons used for $\bar{p}$ cooling.

The advantages of a harmonic over a square well are (1) it is known that the particles can be stored for longer than that obtained with square-well traps (2) the axial length of the antiproton cloud increases automatically when the plasma is radially compressed; this helps suppress the

[1] Musashi Miyamoto (1584-1654) was a well known Japanese Samurai/Zen-philosopher, famous for many duels as well as for his book, 'Go Rin Sho' (Book of Five Rings). In the present context, MUSASHI stands for "Monoenergetic Ultra Slow Antiproton Source for High-precision Investigations"

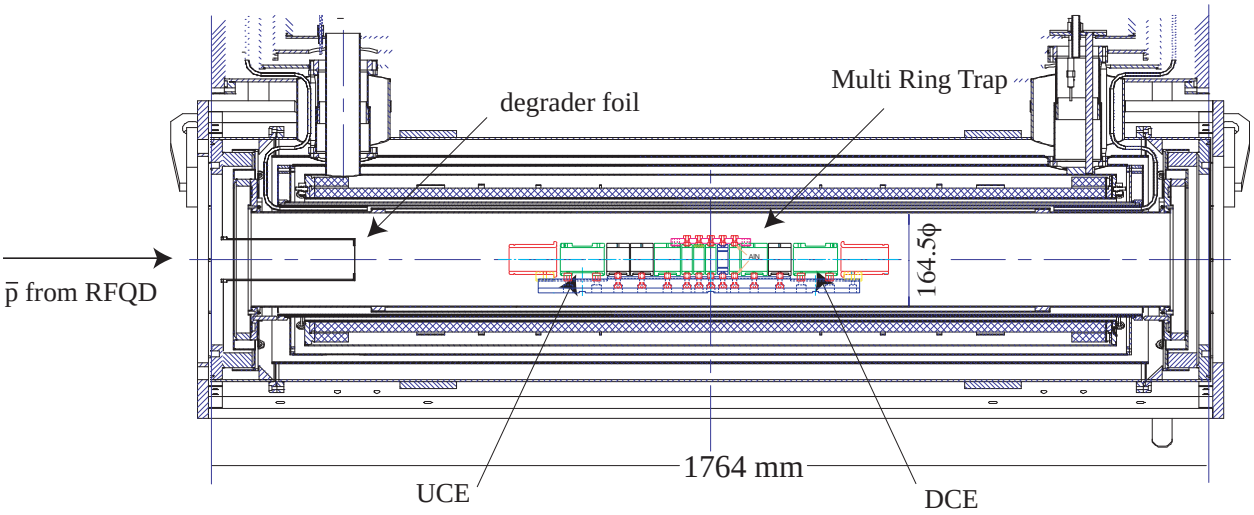

Figure 12: *The configuration of the superconducting solenoid together with the MRT and the degrader foil in the solenoid*

plasma heating, and (3) the axial motion of the cloud allows non-destructive monitoring of the number of trapped particles and the plasma 'temperature' for diagnostic purposes.

By pre-loading the trap with some $\sim 3 \times 10^8$ electrons , which cool themselves via synchrotron radiation with a time constant $\tau_{rad} \sim 0.3$ s at 5T, the trapped antiprotons can be sympathetically cooled via thermal mixing.

2.1.2 Antiproton annihilation detectors for monitoring the $\bar{p}$ behavior in the trap

Two kinds of antiproton annihilation detectors, Čerenkov counters and scintillation counters were used to monitor when and where the antiprotons annihilated:

1) Antiprotons lost from the 200 ns antiproton bunches as they enter, pass through, or leave the trap produce similarly bunched annihilation products. These annihilations constitute important diagnostics of the trapping efficiency. They can easily be detected in Čerenkov counters as an analogue pulse made up of a multitude of individually unresolved annihilations, as in our antiprotonic helium experiments (see section 1.1.1 above). Two such counters were therefore placed at the upstream and downstream ends of the superconducing solenoid, and gave analogue pulses proportional to the antiproton pulse intensity. These were recorded by a digital oscilloscope (Fig. 13).

2) The fact that antiprotons have been successfully enclosed within the trap is signalled by the appearance of individually resolved annihilations. These can occur both on residual gas atoms and on the trap walls. We detected these with a 'track detector' consisting of two 2 m-long plastic scintillator bars, each viewed by two photomultipliers attached at both ends, placed near and parallel to the beam axis. Hit positions of the particles emitted from antiproton annihilation vertices (mostly charged pions) on each of the two scintillator bars were deduced from the timing signals, and the annihilation vertices (projected on the beam axis) were reconstructed. From the event-by-event recording of the track detector signal, the time dependence of the annihilation position distribution was obtained (see Fig. 14).

Another track detector system similar to the one just described, was later installed alongside the extraction beamline (shown in the picture of Fig. 15).

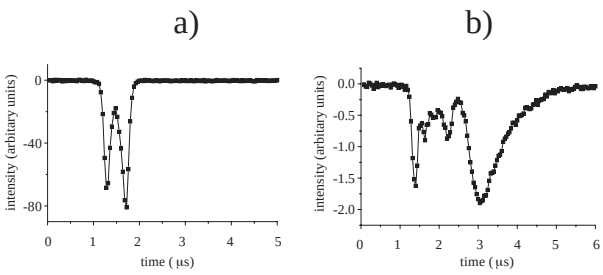

Figure 13: *The output signals of (a)upstream Čerenkov counter with the upstream gate valve closed and (b) downstream Čerenkov counter with the upstream gate valve open.*

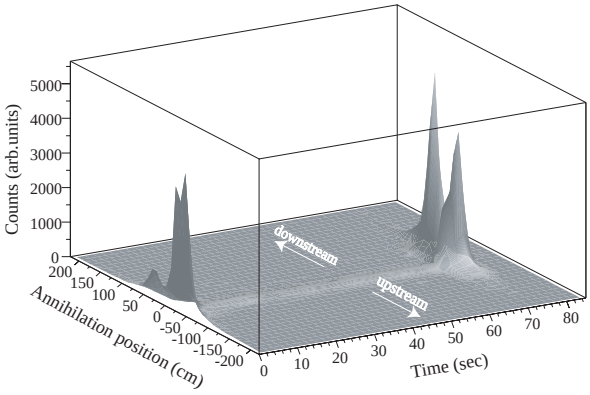

Figure 14: *The annihilation position of antiprotons during injection ($t = 0$), trapping ($0 < t < 70$), and dump ($t = 70$) as a function of trapping time. The center of the trap is at -25 cm in this plot.*

2.1.3 Successful trapping of $> 10^6$ antiprotons

Figure 13(a) shows the time dependence of the $\bar{p}$ annihilation rate when the gate valve at the entrance of the solenoid was closed (all the antiprotons annihilating on or upstream of the gate valve). The peak at $\sim 1.7\mu$s corresponds to antiprotons decelerated in the RFQD, while earlier the sharp peak at $\sim 1.3\mu$s is due to the 5 MeV antiprotons transported through the RFQD without being decelerated.

When the upstream gate valve was opened and antiprotons were allowed to enter the trap, the down-stream Čerenkov detector recorded a spectrum shown in Figure 13(b). Again, a sharp peak at $\sim 1.4\mu$s corresponds to non-decelerated 5 MeV antiprotons, while the second peak at $\sim 3\mu$s is due to the decelerated component annihilating on the gate valve at the exit end of the solenoid. The second peak is now broader because of the energy straggling of the slow antiprotons in the thin degrader foil. When the DCE was biased to -10 kV (*i.e.* when the trapping mechanism operates, as described above) the tail of the second peak was reduced, indicating that the lower energy (< 10 keV) antiprotons were reflected back upstream. This was confirmed by observing an additional delayed peak in the upstream Čerenkov counter spectrum, which is due to the annihilation of the reflected antiprotons returned to the degrader foil [29].

As stated above, applying -10 kV to the UCE before the antiprotons return to it ensures that the particles are confined within the trap volume. The maximum trapping efficiency of $\sim 10\%$ was achieved with an RFQD extraction energy of 97 keV and with UCE and DCE voltages of -10 keV. In this case, about 1.5×10^6 antiprotons were trapped per AD shot. This, the largest number ever achieved at AD or elsewhere, was nevertheless about between 1/4 and 1/3 of what we expected; more optimization work will therefore be required in 2002 to achieve the design figure.

2.1.4 Successful cooling of antiprotons

Figure 14 shows a typical annihilation position distribution as a function of time, measured by the track detector discussed above. In this particular case, electrons were preloaded in the trap, and antiproton were injected in the trap at $t = 0$. After keeping the antiprotons for 70 s in the trap, the trap was 'opened' (the DCE voltage was ramped to 0 V). The bore and the trap were cooled

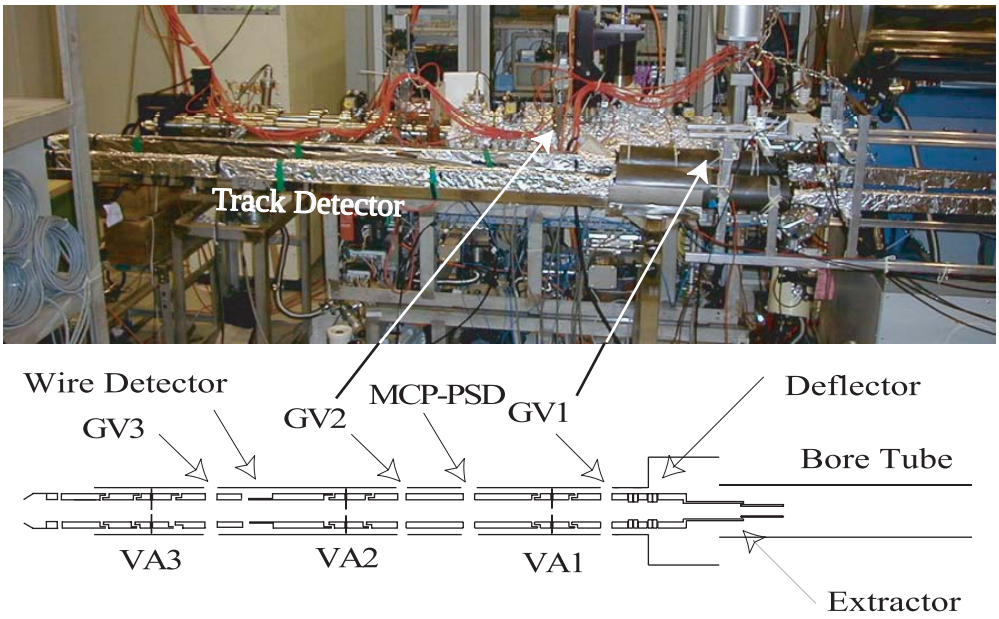

Figure 15: *The configuration of the beam transport elements for ultra slow antiproton beams (lower). The upper part shows the photo of the beamline together with a track detector for the beamline. GV stands for gate valve, VA for variable aperture and MCP-PSD for microchannel plate position sensitive detector.*

below ~ 10 K.

The observed boil-off lasted only for a few seconds, indicating that efficient cooling of the antiprotons by the electrons. During the trapping period, weak but steady annihilations were observed at the center of the MRT, these being due to antiproton collisions with residual gas. The lifetime of the trapped antiprotons was measured to be $\sim 10^3$ s, more than 10 times longer than the AD cycle .

2.2 Extraction

The system transporting the cooled antiprotons extracted from the trap to the to the collision region is required to:

1. have high extraction efficiency between 10 and 1500 eV.
2. compensate for the beam divergence produced by the strongly-divergent magnetic field at the solenoid exit. This required an electrostatic lens system.
3. maintain a pressure difference of more than 6 orders of magnitudes between the trap and the gas jet target through differential pumping.

The lower half of Fig. 15 shows the arrangement of transport elements which realizes the above requirements. To optimize the transport efficiency, the antiprotons are transported at around 250 eV, the final extraction energy being adjusted at the end of the beam line. Two sets of x-y deflectors are placed in the extractor, which enable fine adjustments of the beam position as well as its direction. Downstream of the extractor, two Einzel lenses and one asymmetric lens are installed.

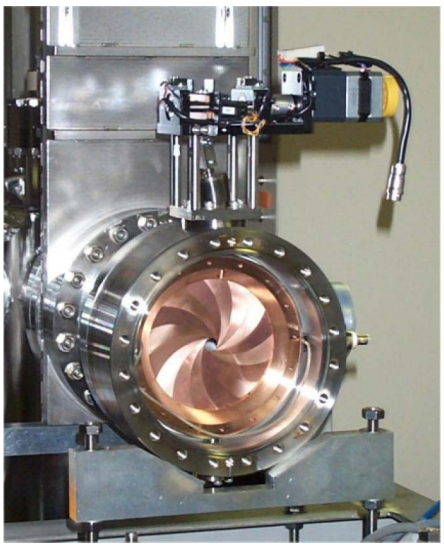

Figure 16: *A photo of the variable aperture, which allows high transport efficiency of antiprotons keeping the differential pumping of more than 6 orders of magnitudes.*

They operate in "acceleration mode", under which the antiprotons are sharply focused at the center of each lens, so that a small variable aperture (Fig. 16) can be inserted at each lens position (VA1, VA2, and VA3 in Fig. 15). The beamline was designed to accommodate three gate valves at ground potential in the three 40 mm gaps denoted as GV1, GV2, and GV3.

Two types of beam profile monitors (BPM) have been developed for diagnostic purposes in this beam line. The first is a position-sensitive detector consisting of a microchannel plate and a delay line (MCP-PSD). As this is a destructive beam monitor, it must be remotely retracted from the beam axis when not in use. This MCP-PSD is sensitive enough to detect a single antiproton, and monitors the beam profile during DC (quasi-continuous) extraction. The second BPM is a multiwire secondary-electron emission chamber for pulsed mode extraction, and contains so little material that the antiproton pulse passes through it without being destroyed. It can therefore remain permanently in the beamline.

Monoenergetic antiprotons in the range from 10 to 250 eV were successfully transported down to the position of the supersonic gas jet (see Section 6) with the spot size of several mm (measured with the MCP-PSD), in agreement with the design value.

The fact that only several thousand antiprotons were transported to the end of the beamline indicates that only $\sim 1\%$ of the trapped antiproton sample is delivered to its final destination. Position distributions of annihilated antiprotons along the beamline obtained with the second track detector placed along the extraction beam line strongly indicate that the radial distribution of antiprotons in the trap was much larger than was anticipated.

In order to improve the transport efficiency, the antiproton plasma in the MRT will be radially compressed by applying a rotating electric field [26]. An extraction scheme to produce microbunches of pulse widths 500-1000 ns with 10 Hz repetition rate, which may be accelerated up to 50 keV is also under preparation.

3 Experimental Progress in Determining the Energy Loss of Slow Antiprotons

The energy loss is an important aspect of the interaction between energetic charged particles and matter. It is therefore important to understand the mechanisms responsible for this energy loss, and to be able to create good theoretical models which can lead to accurate calculations. For this, we need "benchmark" experimental data. Antiprotons are "ideal projectiles" for this purpose, since complications such as lack of charge integrity (protons) and deflection (electrons) are absent.

For projectile velocities much larger than those of the target electrons, the energy loss is well known: It is given by the so-called Bethe equation[30], which gives an energy loss proportional to the projectile charge squared, combined with higher-order terms, which account for non-perturbative mechanisms. The first of these terms is called the Barkas term, and leads to the by now well known marked difference between the energy loss of equivelocity projectiles of opposite charge[30].

At projectile velocities around and below those of the target electrons the theoretical situation is not so clear. Here, a model in which the target electrons are treated as an electron gas, and the energy loss is due to a kind of "friction", gives an energy loss proportional to the projectile velocity. It is also possible to regard the electrons as bound in harmonic oscillators to the target atoms[31]. Quite recently, and spurred by our preliminary measurements with antiprotons, a "binary-encounter" model has been developed[32], which regards the projectile-target electron collisions as separate, but takes into account their non-perturbative nature via an effective potential. This model seems to be very successful, as will be shown in the following.

3.1 May 2001 run.

In May 2001 we had beamtime with the so-called ESA apparatus, which is shown in Figure 17. The apparatus was placed after the decelerating RFQ, which delivers antiprotons of energies in the order of tens of keV. In our apparatus we select antiprotons of a suitable energy in the first electrostatic analyser, let them penetrate a thin target foil, and then the resulting energy is measured by the second analyser. The target can be biased to -25 kV which means that we can measure the energy loss of very low energy antiprotons, even though we transport them through the analysers at much higher energy before and after they pass through the target foil region. This apparatus, as well as the proton measurements with which it was tested is described in reference [33].

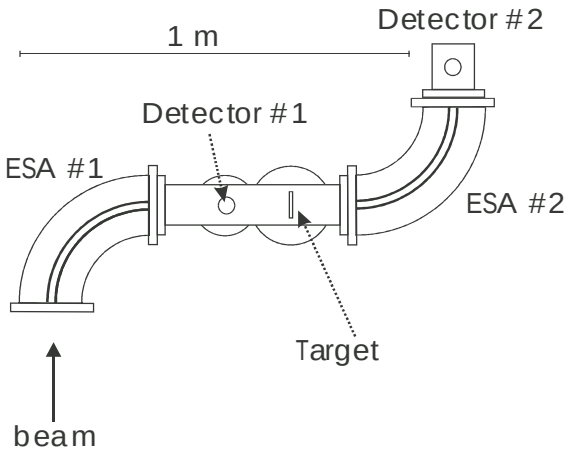

Figure 17: *The ESA apparatus shown schematically.*

3.2 Experimental results

During the May run we obtained experimental data for the energy loss of antiprotons with energies as low as 1 keV in C, Al, Ni, Au and LiF targets. This is approximately a factor of 30 lower energy than we were able to reach at LEAR, and it brings us comfortably into the regime where the projectile is much slower than the target electrons with which it collides. Figure 18 shows our results for the carbon target. As can be seen, the proton data, which we took in Aarhus to test the apparatus, agree very well with the "recommended" curve from the ICRU report (upper solid curve) [34]. The antiproton stopping power is found to be less than half that of the proton stopping power at the lowest energies. As can be seen, the recent "binary encounter" theory reproduces our antiproton data well .

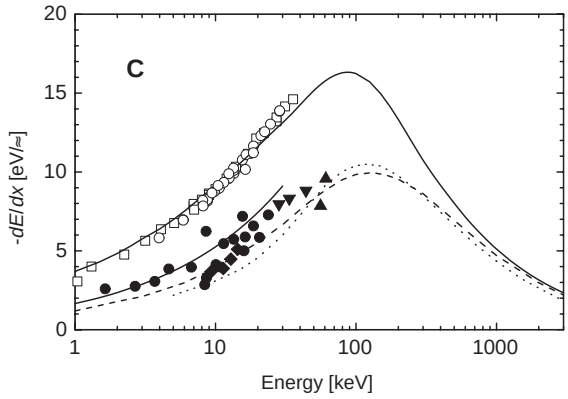

Figure 18: *Experimental results for protons (open symbols) and antiprotons (fillede symbols) on carbon.*

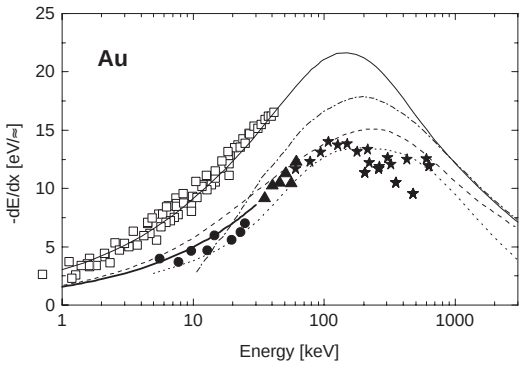

Figure 19: *Data for proton and antiproton stopping power in gold.*

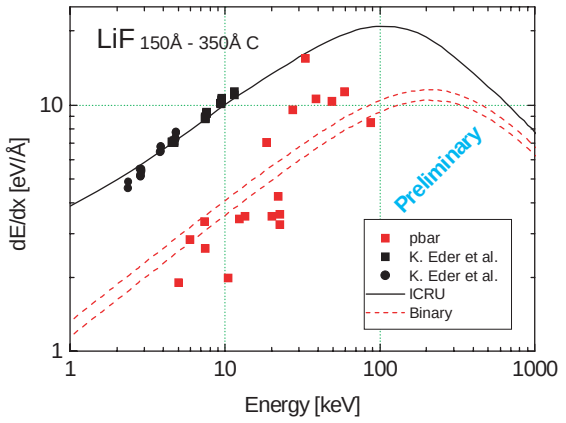

Figure 20: *Data for LiF.*

Figure 19 shows our data for gold targets. Again, the proton data confirm the proper working of our apparatus. The antiproton data are in nice agreement with the new binary-encounter calculations (dashed curve), and also agree with those based on the electron gas model (lower full-drawn curve). They disagree, however, with the results of the harmonic oscillator model (dash-dotted curve). We are therefore able to discriminate between the various models for energy loss. Our data for aluminium and nickel show the same general tendency.

In order to investigate the influence of the target electronic structure on the stopping power, we also used a LiF target, which is an insulator. It has been debated whether the absence of "free" valence electrons in such cases may lead to the energy loss not being proportional to the projectile velocity. Figure 20 shows our results, plotted on a logarithmic scale to emphasize this point. As can be seen, there is an indication that the antiproton data increase with velocity faster that the velocity-proportionality inherent in the binary encounter result.

However, it can also be seen that our experimental data show a great deal of scatter from point to point. This is due to the fact that the beam delivered from the AD was quite unstable with

respect to its transverse position at the entrance to the RFQD and also at the entrance to our apparatus. This problem was solved by the AD operators *after* our run. We are convinced that we can get much better data with the resulting more stable beam.

An important aspect of the slowing down of energetic charged particles in matter is the statistical nature of the process, which leads to a broadening of the energy distribution of the projectiles, the so-called "straggling" in energy loss. In our measurement, we are able to obtain the energy distribution of the projectiles. In figure 21 is shown an example of the width of our measured distributions, in the case of a gold target. Here we have corrected for the width of the energy distribution of the incoming projectiles. As can be seen, the proton data agree well with the upper curve which is the sum of an electron gas calculation by Wang and Ma[35], a contribution from the effect of the bunching of the target electrons into atoms, and an assumed 10% target inhomogeneity. Because of the large scatter of the antiproton data, we have taken mean values of the widths of a number of the measured distributions. These results are also seen in figure 21. They seem to agree with the proton results, although we need better data to be more specific.

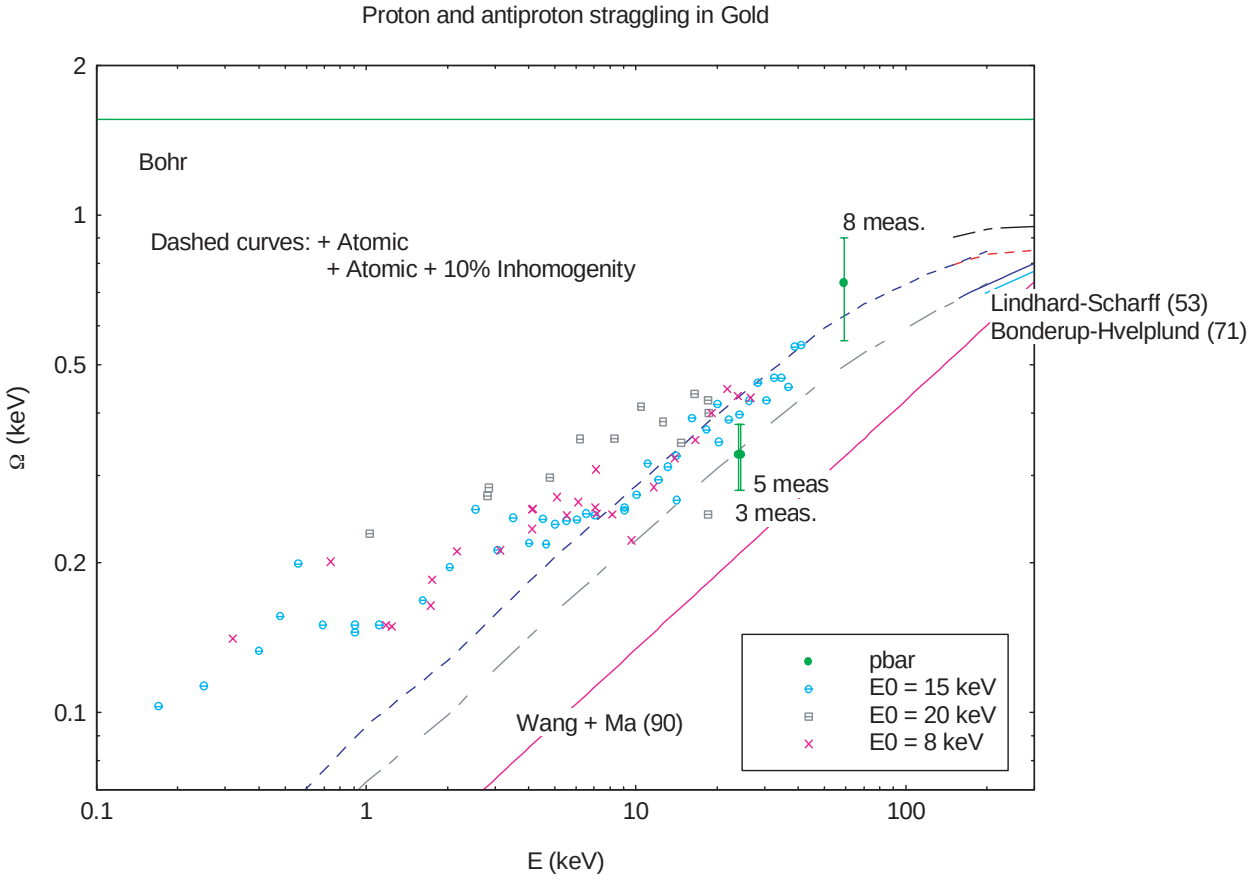

Figure 21: *The width of the energy loss distributions for a gold target.*

3.3 Conclusion :

In our May run, we lost a lot of time due to the fact that the energy of the AD beam was shifted from the value given by the operators. This meant that the RFQD was not working properly.

When this problem was solved, the beam was still very unstable in position. Nevertheless, we were able to obtain the data shown above during our last week of beam time. Two days after our beam time, the AD staff solved the problem with the beam stability. The main conclusion is that we have already obtained good data. However, it is clear that we can get much better data given one week of effective beam time with the stable beam of proper energy as it is now.

Our results for the metallic targets have been submitted to Physical Review Letters (Nov 2001)[3].

Part 2: ASACUSA Plans for 2002

Fig. 22 shows ASASUCA beam time usage plans for 2002.

Weeks 21-24 (Phase 3 development) Ultra low energy beam development - efficiency optimization, etc.

Weeks 25-28 (Phase 2) Stopping power measurement. As shown in Part 1, due to the poor machine condition during the stopping power measurement in 2001, a part of the programme had to be deferred, and will be completed in 2002.

Weeks 29-34 (Phase 1 & 2) Laser spectroscopic study of $\overline{\mathrm{p}}\mathrm{He}^+$ interaction with other atoms and molecules, and development of $\overline{\mathrm{p}}\mathrm{He}^+$ two-photon laser resonance spectroscopy. The latter is an important step towards achieving 10^{-9} precision in antiproton mass and charge. More description in Section 4.

Weeks 35-39 (Phase 3) Protonium production by collision of ultra slow antiprotons on a molecular hydrogen gas jet target, the first step towards protonium laser spectroscopy. Described in detail in Section 6.

Weeks 40-43 (Phase 3) Ionization of atomic hydrogen by slow antiprotons. It is known that the simplest three-body collision, $\bar{p} + \mathrm{H} \rightarrow \bar{p} + p + e^-$, is theoretically difficult to handle, and theoretical predictions start to diverge below the energy where the experimental data cease to exist. Our Phase 3 measurement will provide valuable benchmark data. More description in Section 5.

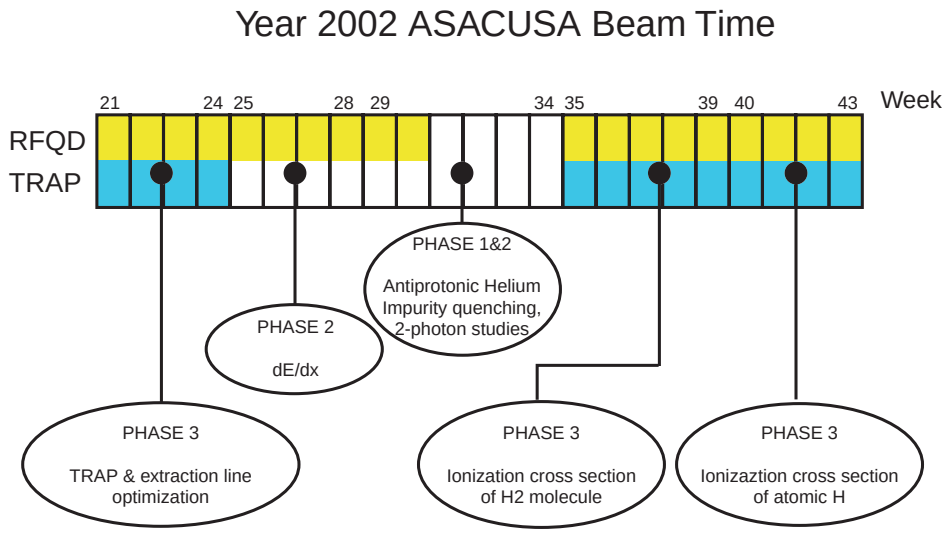

Figure 22: *ASACUSA 2002 Plans.*

4 $\overline{\mathrm{p}}\mathrm{He}^+$ Spectroscopy

In year 2002, we plan to complete the following:

1. Study of quenching of $\overline{\mathrm{p}}\mathrm{He}^+$ by hydrogen, deuterium and other molecules (phase 1 setup).

   The fact that hydrogen (and deuterium) molecules have large (n,l)-dependent quenching cross sections was used already to find many *metastable-to-metastable* laser transitions, by selectively quenching the larger-n level by adding a small amount of hydrogen (deuterium) into the target helium[36, 37, 38, 39].

   The (n,l)-dependent quenching collisions of $\overline{\mathrm{p}}\mathrm{He}^+$ on hydrogen has attracted attentions of quantum chemists. Recent *ab initio* calculations [40] indicate the existence of a barrier in the interatomic potential of $\overline{\mathrm{p}}\mathrm{He}^+$ and H_2, whose height increases for decreasing n, in qualitative agreement with the observed (n,l) dependence of quenching cross section. However, these calculations fail to explain the *isotope* dependence, i.e., the difference in hydrogen and deuterium quenching cross sections.

   In 2002, we will measure the temperature dependence of the $\overline{\mathrm{p}}\mathrm{He}^+$–$H_2$ and $\overline{\mathrm{p}}\mathrm{He}^+$–$D_2$ quenching cross sections in order to deduce the potential barrier heights for each (n,l) state.

2. Doppler-free two-photon spectroscopy of $\overline{\mathrm{p}}\mathrm{He}^+$ (phase 1 setup).

   As will be described in Sec. 7, elimination of the Doppler widths will be needed in our future $\overline{\mathrm{p}}\mathrm{He}^+$ spectroscopy aiming at ∼ppb precision. In 2002, a proof-of-principle measurement will be done by using two counter-propagating laser beams of, for example, 529 nm and 470 nm, inducing a Doppler-free $E2$ transition from $(n,l) = (38,35)$ to $(36,33)$. 5.3 MeV antiprotons will be stopped in a room temperature cell at 3–5 bar helium pressure so that the Doppler broadening will exceed the line width of $0.6 \ldots 0.8$ GHz of our current pulsed laser system.

3. High precision $\overline{\mathrm{p}}\mathrm{He}^+$ spectroscopy at very low helium densities using the RFQD and a spectrometer line (phase 2).

   As shown in Sec. 1.3.1, stopping antiprotons from the RFQD in very a low density helium gas target makes it possible to determine $\overline{\mathrm{p}}\mathrm{He}^+$ transition frequencies without the need for the density extrapolation. The data taken in 2001 should already make it possible to improve the $\bar{\mathrm{p}}$ mass and charge CPT limit by a factor 2–3, but better limits can be reached if the background due to the *undecelerated* antiprotons are eliminated. The RFQD transports not only the decelerated antiprotons, but also undecelerated 5.3 MeV antiprotons quite efficiently. These antiprotons penetrate the low-density helium target, stop in the down-stream quartz window, annihilate, and produce a 2.2 μs continuum background due to the $\pi - \mu - e$ decay chain, which is difficult to eliminate. Shot-to-shot spatial variation of the antiproton beam spot at the entrance of the RFQD causes signal-to-noise ratio of the laser resonance spike to fluctuate, which contributes to the systematic error of our measurement.

   Therefore, in 2002, we plan to install an achromatic beam transport between the RFQD and the low-density target so that only the decelerated antiprotons enter the target, and study in detail how this helps reduce the systematic error.

4. Search for prolonged lifetime of antiprotons in helium at ultra-low density (phase 2 setup)

   An open question so far is the missing population of states with $n > 40$ as compared to theoretical predictions (cf. sec. 1.3.3). With reduced background after the spectrometer line we hope to be more sensitive to observing changes of the time spectrum at ultra-low density.

If no change in lifetime is observed, we can try to induce laser transitions from the highest populated states upwards. If the description of Sauge and Valiron [40] is correct, states at $n > 40$ have vanishing inter-atomic barriers and should therefore be short-lived. In this case we should be able to observed upwards transitions like in the HAIR and DAIR case. If Korenman [21] is right and the high-lying states are destroyed during the thermalization stage, such transitions should not be visible.

At very low densities we may also observe a change in the lifetime of the $\overline{\mathrm{p}}\mathrm{He}^{++}$. In a normal laser transition, the $\overline{\mathrm{p}}\mathrm{He}^{++}$ that is formed after an Auger transition is immediately destroyed by Stark mixing in collisions, and the laser spike decays with the Auger lifetime ($\leq$ 10 ns) of the daughter sate of a transition. A reduction of the Stark mixing at very low densities will result in a slower decay of the laser spike, which would allow the direct determination of Stark mixing rates.

5 Ionization in Collisions of Slow Antiprotons and Atoms

Atomic collisions between point-like charged particles and few-electron atoms are very fundamental processes. Nevertheless, our ability to calculate accurately the outcome of such collisions is still limited, due to the complexity of the dynamic many-body processes involved. Supplied with proper benchmark experimental data on such collisions, however, theorists can test their models for the solution of the dynamic 3-body problem and the influence of electron – electron correlation.

These systems are especially interesting at low projectile velocities, where the interactions are non-perturbative.

To get at as simple systems as possible, we should use atomic hydrogen or helium as targets, since then the number of "spectator" electrons is minimized. Nevertheless, other targets are also of interest. To avoid complications connected with the interchange of electrons between the projectile and the target, we should use antiprotons as projectiles, since they do not carry bound electrons. In this case, there are even more benefits if we compare with the option of using electron projectiles: There are no electron-exchange effects and the projectile orbits are "classical".

Therefore, the antiproton is the theorists "dream projectile" in such investigations.

We have constructed an apparatus with which we plan to measure the ionization cross section of atomic hydrogen, helium and other targets for impact of antiprotons in the range where the projectile velocity is lower than that of the target electrons, i. e. below 25 keV.

5.1 Ionization

Until now, we have obtained data on the ionization of atoms (and molecules) for impact of antiprotons with energies from 20 MeV down to 30 keV in the case of atomic hydrogen[41] and 13 keV in the case of helium target[42]. This work covers the case where the projectile is "fast" compared with the target electrons. As examples of the results, figures 23 and 24 show our data for atomic hydrogen and helium. They are compared with a number of theoretical calculations. Clearly there is hardly any agreement between the various calculations in the case where slow collisions are considered (below, say 25 keV). In the case of the helium target, where we have been able to measure down to 13 keV, furthermore, the theoretical calculations do not agree with the experimental data. Clearly, there is a need to obtain benchmark data in the projectile range of 1 – 25 keV in order to guide the theorists.

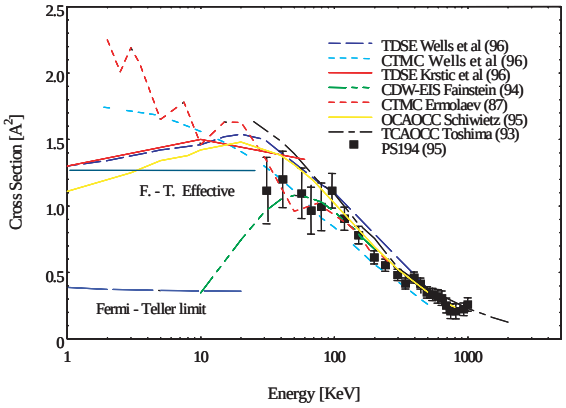

Figure 23: *The cross section for ionization or atomic hydrogen by antiproton impact as measured by the PS194 collaboration at LEAR.*

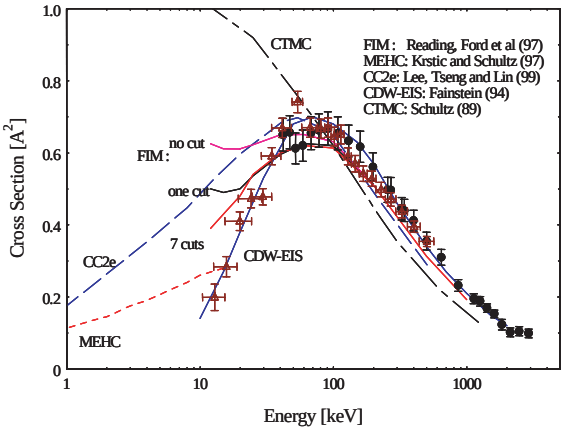

Figure 24: *The cross section for single ionization of helium by impact of antiprotons. The points show our data taken at LEAR.*

5.2 Experimental apparatus.

The experimental apparatus and method is based on our previous experience from our work at LEAR. Figure 25 shows a simulation of an antiproton beam which crosses a thermal beam of atomic deuterium in the central part of our apparatus. Here, D^+ ions are created via ionization, and they are extracted and focussed onto a microchannel-plate detector. The antiprotons are detected downstream by another microchannel-plate detector, and the time difference between the pulses in these two detectors gives the ion time-of-flight, which again let us discern between D^+ and other ions. The apparatus is designed so as to accept the angular scattering of the projectiles as well as the recoil of the target atoms. There is, however a limit to this acceptance, so that we expect to be able to measure down to antiproton energies in the order of a few keV.

Figure 26 shows the design in more detail. The antiprotons come from the ASACUSA catcher trap from where they are extracted as a 1 keV DC (quasi-continuous) beam through a differentially pumped extraction beam line. To get at other collision energies, the entire collision chamber (right part in Fig. 26) can be floated to 20 kV.

The target consist of a thermal jet of either atomic deuterium or other gases such as helium. The atomic deuterium is created in a microwave source situated in a differentially pumped chamber. This source, which was constructed at Queens University of Belfast has already been tested. It has a dissociation fraction of better than 90%, and delivers a density of 10^{11} D atoms/cm^3 at the target region.

In order to measure the ionization cross section it is necessary to know the product of detection efficiencies and integrated target density. This we achieve by exchanging the antiproton beam and detector with a pulsed electron gun and a Faraday cup. We are then able to normalize to the well known ionization cross section for fast electron impact. For the case of ionization of atomic deuterium we expect the following signal:

$$N(D^+) = \sigma n l N(\bar{p}) = 10^{-16}\mathrm{cm}^2 \times 10^{11}\mathrm{cm}^{-3} \times 1\mathrm{cm} \times N(\bar{p}) = 10^{-5} N(\bar{p})$$

Since we expect to be able to extract $N(\bar{p}) = 10^6$ from the trap per AD shot this gives $N(D^+) = 10$ per AD shot or 300 per hour. With respect to background signals, these will come mainly from the photons emitted by the hydrogen plasma in the atomic hydrogen source. It is hard to estimate this background. However, similar experiments have succeeded in suppressing in to a tolerable level

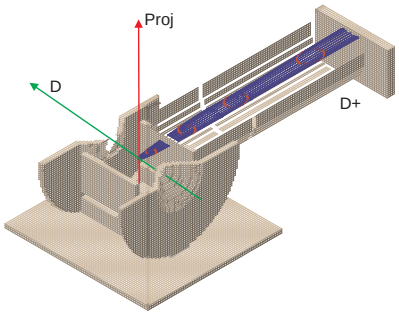

Figure 25: *SIMION simulation of collisions in the central part of our apparatus.*

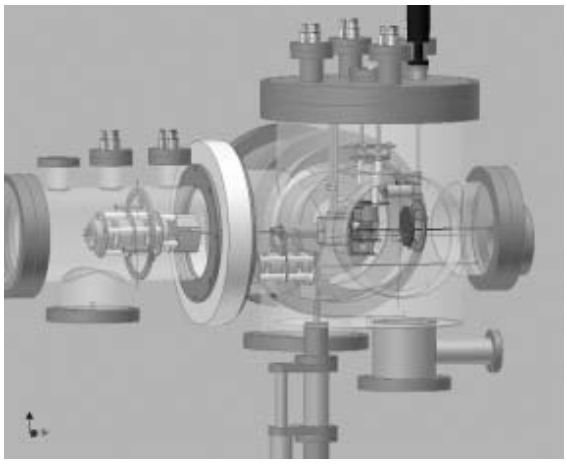

Figure 26: *The experimental apparatus.*

[41, 43, 44] and our apparatus is designed especially to remedy this problem. In the case of other targets, we expect larger signals and less background.

5.3 Status

The atomic hydrogen source has been tested and works as expected. The ion- and beam optics have been simulated. The design is close to designs already used in our experiment at LEAR. The vacuum chamber with is internal structure has been designed, and is promised ready from the Aarhus workshop in January 2002. The connection to the extraction beam line has been designed, and is promised ready from the workshop in February 2002. Tests with protons and electrons are planned for spring / summer 2002.

6 Antiprotonic atom production

The previous section (5) described the results obtained with the RFQD on the atomic interactions of antiprotons at energies down to 1 keV, at which only ionization and excitation take place. By combining the RFQD and MUSASHI, as described in Sec. 2 of Part I, we can now enter a new domain of electronvolt energies, at which antiprotonic atom ($\bar{p}A^+$) formation [45] also comes into play. Furthermore, since it is collisions which destroy these atoms once formed, the lifetimes of varieties such as protonium ($\bar{p}p$) and $\bar{p}He^{++}$ are expected to increase and approach the 'intrinsic' one (*i.e.* the value in vacuo, which has not been reduced by collisions) as the density of the target gas is reduced to zero. Metastability should therefore begin to appear in $\bar{p}p$ at low target pressures, while that already known in $\bar{p}He^{++}$ for high densities should become more pronounced.

An antiproton approaching an atom with kinetic energy $K_{\bar{p}}$ less than about 100 eV does so at a velocity $\sqrt{\frac{2K_{\bar{p}}}{M_{\bar{p}}}} < 4 \times 10^{-4}c$ much lower than the Bohr velocity, $Z_{\rm eff}\alpha c$, of an the atom's outer electrons ($Z_{\rm eff}$ being the screened nuclear charge seen by the electron). Under these conditions the electron's binding energy and orbital speed both fall adiabatically as the antiproton approaches, and it moves further from its nucleus. At the same time the antiproton loses kinetic energy adiabatically; if its initial value is not high enough to compensate for the initial binding energy of the electron, it will remain bound to the target nucleus instead of the electron and an antiprotonic atom will

be formed, otherwise it remains in the continuum itself. The electron release mechanism therefore results either in simple ionization or in antiprotonic atom formation depending on the kinetic energy of the antiproton. The same argument can be made for other "heavy electrons" like μ^-,π^-, and K^- [46].

The thermal energy of the target atoms (25 meV at room temperature) can be neglected in comparison with the initial antiproton kinetic energy; energy conservation before and after the collision in the laboratory system then requires, for the case of antiprotonic atom formation:

$$K_{\bar{p}} - \epsilon_e = K_a + K_e - \epsilon_{\bar{p}} \tag{10}$$

with binding energies $\epsilon_{\bar{p}} \sim \frac{\mu_{\bar{p}}}{m_e} \times \frac{\epsilon_R}{n^2}$ and $\epsilon_e \sim \epsilon_R$.

Here, the K_e and $K_{\bar{p}}$ are the kinetic energies, ϵ_e and $\epsilon_{\bar{p}}$ the binding energies and m_e and $\mu_{\bar{p}}$ the reduced masses, of the electron and the antiproton respectively. ϵ_R is the binding energy of the displaced electron, (equal to the Rydberg energy 13.6 eV for hydrogen). K_a is the recoil energy of the antiprotonic atom.

The adiabatic nature of the collision (*i.e.* negligible momentum carried by the released electron) ensures that the momentum of the antiprotonic atom is practically that of the incident $\bar{p}$, in which case the principal quantum number n of the adiabatically-formed (negligible K_e) atom can be estimated using the above expression for $\epsilon_{\bar{p}}$:

$$n \sim \sqrt{\frac{\mu_{\bar{p}}}{m_e} \times \frac{\epsilon_R}{\epsilon_e - \kappa K_{\bar{p}}}}, \tag{11}$$

where $\kappa = \frac{A}{A+1}$ for a target of mass number A (*e.g.* , $\kappa = 1/2$ for atomic hydrogen and $\kappa \to 1$ for heavier targets). The atoms so prepared then form a high quality beam with the momentum distribution of the incident $\bar{p}$. The antiproton $n-$value is thus a function of $K_{\bar{p}}$ only, and can be tuned from $n_{min}(\sim \sqrt{(\mu_{\bar{p}}/m_e)})$ to ∞ by increasing $K_{\bar{p}}$ from 0 to $\frac{\epsilon_e}{\kappa}$.

6.1 Formation process calculations for protonium

Protonium ($\bar{p}p$) is particularly interesting because it is the simplest hadronic particle/antiparticle system. From the high Rydberg Yrast states populated at formation, it can cascade down only via slow radiative transitions with its lifetime much longer than 1 μsec, at very low target densities such as we are planning, hence high resolution laser spectroscopy of $\bar{p}p$ becomes feasible for the first time. Calculations of the ionization and antiprotonic atom formation cross-sections have been done by Cohen, employing a CTMC (Classical Trajectory Monte Carlo) method and an FMD (Fermion Molecular Dynamics) method for $\bar{p} - H$ and $\bar{p} - H_2$ collisions [47]. The results of are given in Fig. 27. The solid line and the dotted line show protonium formation cross section, $\sigma_{\bar{p}p}$, and total (formation and ionization) cross section, σ_t, in $\bar{p} - H$ collisions, respectively. A clear threshold is seen as the energy falls below 30 eV for $\sigma_{\bar{p}p}$ although σ_t varies smoothly across the threshold, which is the direct consequence of the scenario discussed above that the electron release process is the key process, which ends either as ionization or as antiprotonic atom formation depending on the kinetic energy of the antiproton.

For the case of molecular hydrogen, an antiprotonic molecule will be temporarily formed, which then dissociates into an antiprotonic atom and a residual atom(ion) [47]. The effect can be taken into account in the CTMC calculations, which predict a dramatic increase of $\sigma_{\bar{p}p}$ for H_2 over the quantities for H far above the threshold energy (see Fig. 27).

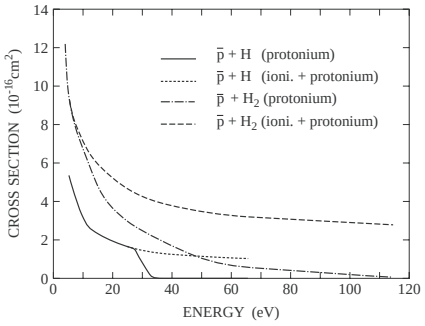

Figure 27: *Total (dashed lines) and capture (solid lines) cross sections of antiprotons in collisions with H (heavy lines) and with H_2 (light lines) atoms evaluated with a CTMC calculation.[47]*

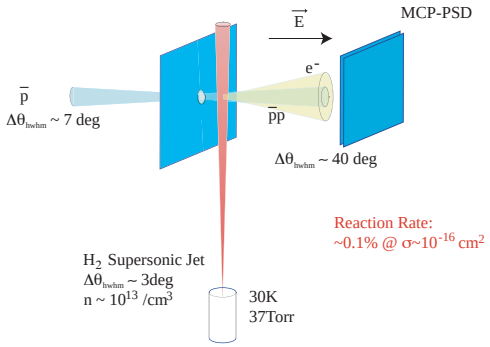

Figure 28: *A schematic drawing of the experimental configuration for antiprotonic atom formation*

6.2 Metastability in multielectron antiprotonic atoms

Various multi-electron antiprotonic atoms are also expected to have intrinsic meta-stability in vacuum when they are prepared under single collision conditions. The CTMC calculation ([23]) shows that $\bar{p}Ne$ can be formed even at relatively high impact energy of antiprotons because multiple electron release process will play an important role, which in itself contains important information of electron-electron correlation at low energy antiproton collisions.

6.3 Practical realisations - the ASACUSA gas-jet target

Figure 28 shows a schematic configuration of the experimental setup. The ultra slow antiproton beam prepared by MUSASHI is injected in the collision region, focused on the supersonic gas jet target, and then is detected by the MCP-PSD. The MCP-PSD detects both the released electron and the antiproton/antiprotonic atom. Because the momentum of $\bar{p}p$ is roughly the same as that of the incident antiproton, i.e., the traveling time of the $\bar{p}p$ from the collision region to the MCP-PSD is a factor of two longer than that of $\bar{p}$, the identification of the collision processes is expected to be straightforward. A molecular hydrogen jet, which provides a high target density, will be used at first, and will in a later phase be supplemented by an atomic one . An MCP-PSD to detect antiprotons and the collision products is installed on one of the two arms in the main chamber, which can rotate around the gas jet.

Figure 29(a) schematically shows the structure of the collision chamber, which consists of the expansion chamber with the gas cell cooled down around 30K, the collimation chamber, the main chamber, and 1st and 2nd dumps of the supersonic gas jet. Figure 29(b) shows a drawing of the collision chamber. The expansion chamber and accordingly the gas cell nozzle are on a XYZ stage and are alignable against the skimmer fixed to the collimation chamber.

The supersonic gas jet nozzle and the gas dump has an ability to prepare H_2 target with a density as high as $1 \times 10^{13}/cm^3$ keeping the collision chamber at 5×10^{-7} Torr, which satisfies the requirements of MUSASHI that the vacuum of the downstream end of the beamline should be better than 10^{-6} Torr. At this target density, the reaction fraction amounts to $\sim 0.1\%$.

The closed gas re-circulation system shown in fig. 30 is under construction to handle the gas jet in accordance with CERN hydrogen safety regulations.

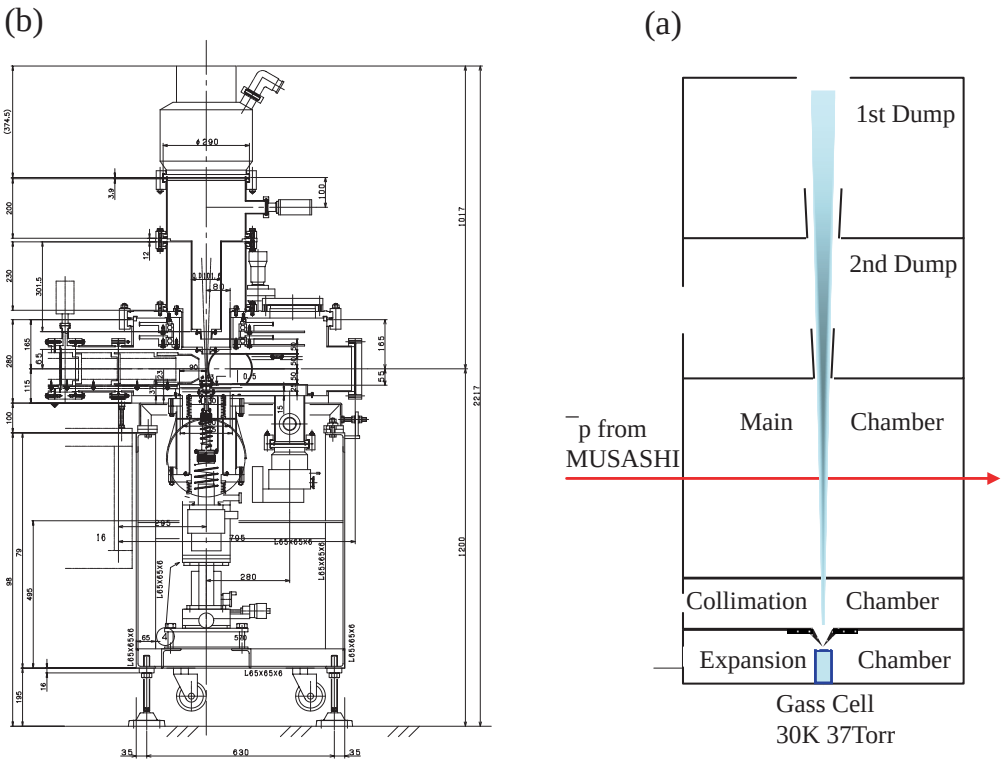

Figure 29: *The drawing of the collision chamber*

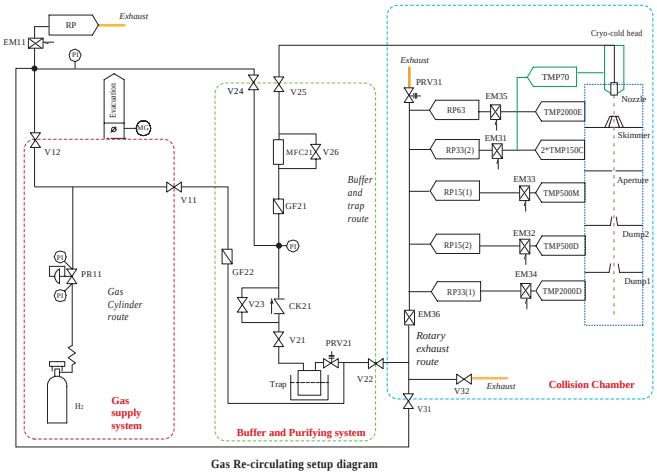

Figure 30: *Gas re-circulation system.*

Part 3: 2003 and beyond

In this part, we describe the three measurements currently being discussed within the collaboration, to be carried out in 2003 and beyond. They are,

1. Sub-ppb Laser Spectroscopy of Antiprotonic Helium. This is a continuation of already quite successful $\overline{\mathrm{p}}\mathrm{He}^+$ spectroscopy. Our next goal is to achieve ~ 1 ppb (10^{-9}) absolute precision. When accomplished, the precision of antiproton mass will surpass that of proton (currently 2.1 ppb). Some technical details are described in Section 7.

2. Ionization of Atoms: Kinematically Complete Experiments. This was already described in our original proposal [1]. Status of preparation is shown in Section 8. The efficiency of such measurements can be dramatically improved by using a ultra low energy $\bar{\mathrm{p}}$ storage ring (not in our original proposal[1]), which is discussed in Section 8.3

3. Measurement of protonium and other X-ray spectra (not in our original proposal[1]). Measurements of antiprotonic X-rays were actively pursued at LEAR, but such measurements are not possible any more at AD because of the lack of slow-extraction capability. ASACUSA's phase 3 infrastructure, trap + extraction beam line, can be used to deliver time-stretched antiproton beams for measurements, such as described in Section 9.

7 Sub-ppb Laser Spectroscopy of Antiprotonic Helium

Figure 31 summarizes various factors which contribute to the absolute precision of $\overline{\mathrm{p}}\mathrm{He}^+$ laser spectroscopy. By using the ~ 50 keV beam from the RFQD, and stopping the antiprotons in a low density (~ 1 mb) helium gas target, as we already did in 2001 and reported above, the first two, collisional shift and broadening, can be largely eliminated.

The first order Doppler width can be completely eliminated by inducing resonant transitions with two counter-propagating laser beams. When this is done, the transition probabilities are usually much smaller than those of single-photon E1 transitions; they are, however, enhanced when an intermediate virtual level is close to a real state, as shown in Fig. 31. The two-photon transition rate will be measured in 2002, in order to confirm the principle of such measurements.

The remaining factor is the laser bandwidth. This can be reduced by more than an order of magnitude if the present pulsed laser system is replaced by pulse-amplified CW one in which the CW laser is locked to a frequency standard (see Fig. 32). Such a laser system is currently being developed by the collaboration.

By combining all these improvements, absolute precision of ~ 1 ppb or better should be achievable within a couple of years.

8 Ionization of Atoms: Kinematically Complete Experiments

The study of ionization of atoms by antiprotons at very low antiproton impact energy, discussed in Section 5 of Part II, will be extended to measurements of differential cross sections by making kinematically complete measurements of the momenta of the ejected particles (*i.e.* the electron(s) and the recoiling ion).

Such kinematically complete experiments for heavy incident particles like the including antiproton have only become feasible since 1995[48, 49, 50, 51, 52, 53], which saw the development of the so-called *Reaction Microscope* imaging technique [54] (Cold Target Recoil Ion Momentum

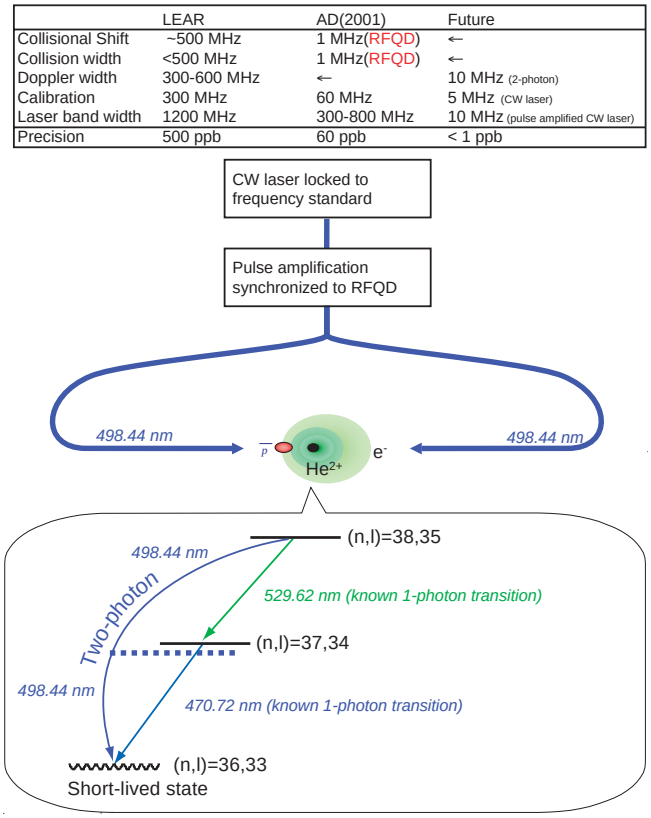

Figure 31: *Precision limiting factors and our plans to reach* 10^{-9} *precision in* $\overline{\mathrm{p}}He^+$ *spectroscopy*

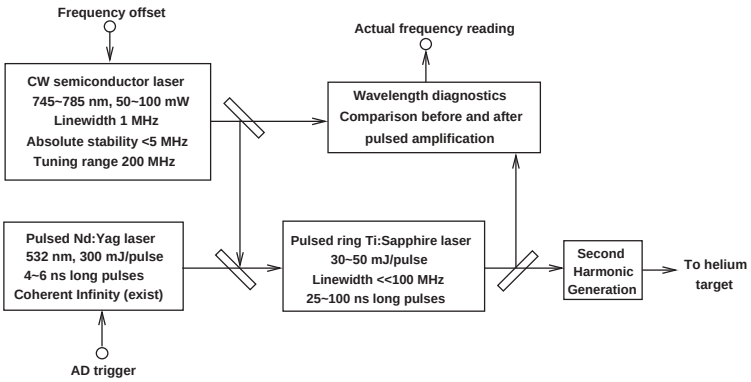

Figure 32: *Pulse-amplified CW laser system being developed for future high-precision* $\overline{\mathrm{p}}He^+$ *spectroscopy.*

Spectroscopy (COLTRIMS)[55]). In these devices, electric and magnetic guiding fields are used to direct ionization electrons and target fragments emerging over a large solid angle onto position sensitive detectors (Fig. 33), thereby making it possible to measure differential cross-sections.

The first such experiment at 945 keV was performed in 1996 at LEAR by the PS 194 collaboration [56], with results in overall agreement with the prediction of CDW (continuum distorted wave) calculations at these high energies, where the collision dynamics is much easier to treat. However, at energies below about 100 keV[57] various recent theoretical approaches revealed substantial differences even in the total ionization cross-section for atomic hydrogen and the single-ionization cross-section for helium. The various theoretical approaches differ by orders of magnitude, and they all contradict the differential cross-section measurements for fast heavy-ion impact[51] (Fig. 34). Furthermore, for low-energy (10 to 15 keV) antiproton impacts, characteristic features have been found in the electron emission cross sections [58] which are not yet explained quantitatively by any theory.

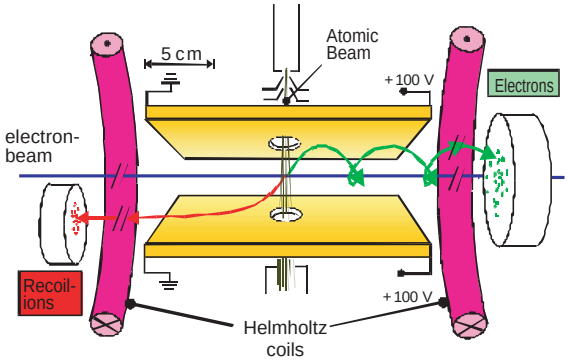

Figure 33: *Schematic of the Reaction Microscope. For details see [54]*

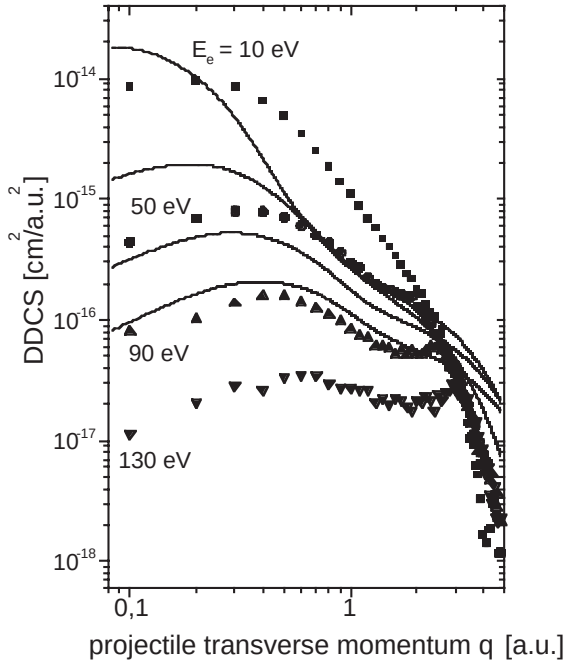

Figure 34: *The doubly differential cross section* $\mathrm{d}^2/(\mathrm{d}q_\perp \mathrm{d}E_e)$ *as a function of the projectile transverse momentum transfer* $q_\perp$ *for specified and fixed electron energies* E_e *for single ionization of helium by 100 MeV/u* C^{6+} *impact. Full symbols: experiment. Solid lines: theoretical results. For details see [51].*

We therefore intend to perform kinematically complete experiments on single ionization of hydrogen and helium by antiprotons with energies between 5 keV and 50 keV. Measurements on these, the most fundamental three-particle reactions in atomic physics, will provide urgently required benchmark data for theory at low velocities.

8.1 Mid-term running plan: Status of preparation

The reaction microscope of Fig. 35 has been developed, optimized and tested in various experiments on single ionization of helium by positively charged ions under conditions similar to those for low-energy antiprotons. It features many improvements over the one used in the LEAR experiment. Thus, the background pressure (*i.e.* the quality of the vacuum outside the jet) has been considerably reduced, and the momentum resolution improved by optimising the extraction field and pre-cooling the target gas before expansion. In test experiments on single electron capture reactions, we have achieved a previously unsurpassed momentum resolution of 0.07 a.u. in the most important (*i.e.* longitudinal) direction (Fig. 36). To reach very low energies ($\leq$ 5 keV) the electrons and ions are now extracted longitudinally (*i.e.* along the incoming antiproton-beam direction) instead of transversally as in the LEAR experiment. A test run with slow 7 keV/q Ne^{7+} beams at our Electron Beam Ion Trap (EBIT) has demonstrated that with longitudinally-directed fields, even very low-energy antiproton beams can be easily transported through the reaction microscope.

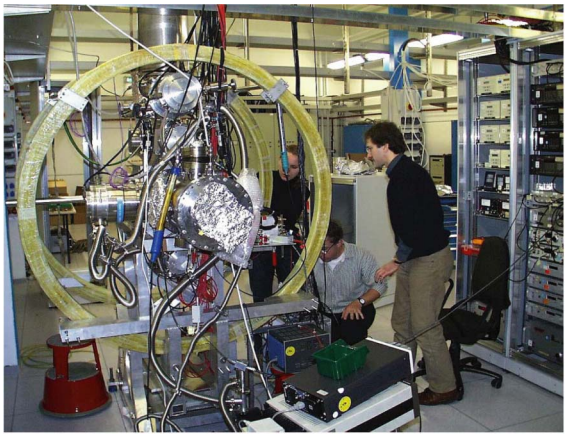

Figure 35: *New reaction microscope with three-stage cooled super-sonic gas-jet.*

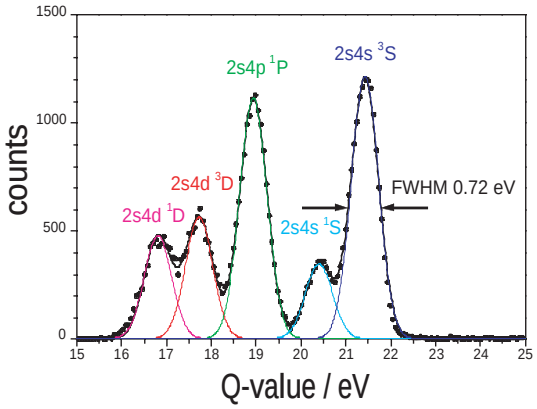

Figure 36: *Longitudinal recoil-ion momentum spectrum $P_z = Q/v_P$ converted into the $Q-$value of the reaction for single capture in Ne^{7+} on He collisions at a projectile velocity $v_P = 0.4$ a.u.. The momentum resolution in 0.007 a.u.*

A final test of our apparatus will be performed at the end of 2001 using a fast proton beam at the Max-Planck-Institut für Kernphysik. We expect the apparatus to be fully operational for the investigation of antiproton collisions within the second half of 2002. At least 10^5 antiprotons per second, focussed on a 1 mm diameter spot, will be needed to be able to get results with reasonable statistical significance.

8.2 Long-term perspectives: Multiple ionization using an electrostatic storage ring.

With antiproton fluxes $\leq 10^5$/s (as achieved with the AD, RFQ and ASACUSA trap) focussed onto the 1 mm diameter target of the reaction microscope, the most interesting differential experiments on double or multiple ionization of helium and other atoms/molecules unfortunately remain unfeasible. One way of doing these experiments in the future would be to store the slowed-down antiproton bunches in a small electrostatic ring into which a reaction microscope is integrated, thus increasing the present luminosity by about five orders of magnitude. Such an arrangement

would, for the first time, allow to systematically explore fundamental many-particle dynamics in the interaction of antiparticles with matter.

Accordingly, a collaboration between the University of Aarhus, the Frankfurt University and the Max-Planck-Institut für Kernphysik has made a proposal (Bundesministerium für Bildung und Forschung, BMBF)[59] to design, build and test such ring-microscope, based on technical specifications close to those of the existing ELISA storage ring in Aarhus[60]. While work on the reaction microscope was supported, the funding of the electrostatic storage ring itself was delayed. We have now completed the design and the construction of this reaction microscope (Fig. 37) and will test it in 2002 for implementation into the ESR storage ring at the end of that year. At the same time, the Frankfurt/Aarhus group has started to design an electrostatic storage ring suitable for antiproton energies between 1 and 100 keV, with a circumference of about 10 m. Given a positive funding decision, this could become operational by 2004.

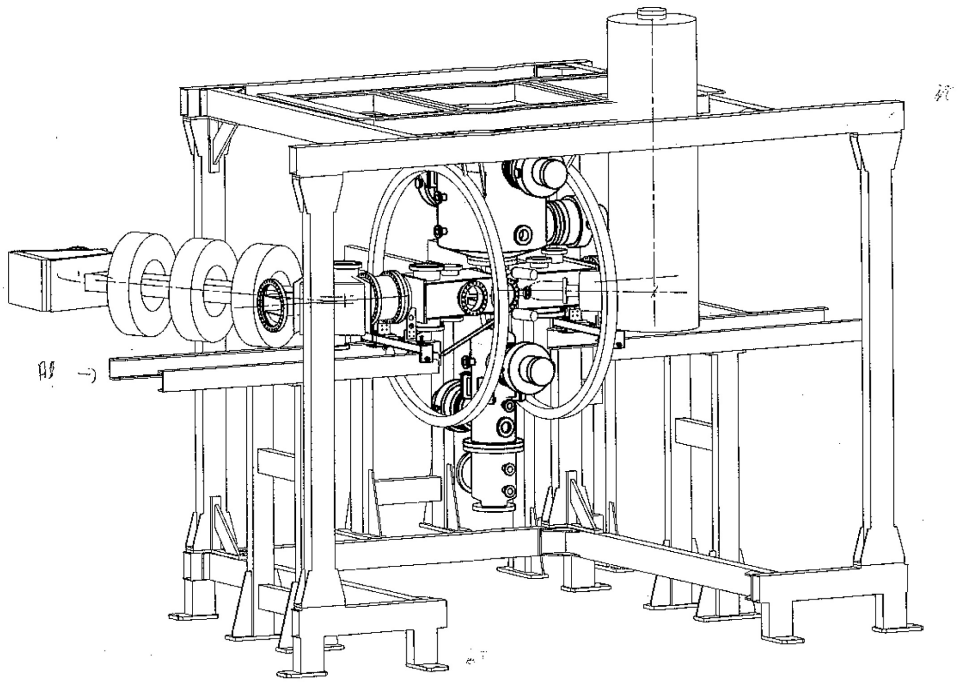

Figure 37: *New REACTION MICROSCOPE especially designed to be implemented into a storage ring. The apparatus will become operational at the end of 2001.*

8.3 Table top $\bar{p}$ storage ring

A small-scale charged particle electrostatic storage ring for ions, leptons, molecules etc. in the keV/u range is under construction at the Frankfurt university, and should be capable of storing antiprotons between 1 to 100 keV. Only electrostatic deflection and focusing elements are used. Of similar design to ELISA, it is small enough to be transported (e.g. on a truck) as operating unit to different research labs, (e.g. from Frankfurt to AD/CERN or BESSY II).

This is schematically shown in Fig. 38. The ring is approximately square, with focusing (QD/F) and deflection elements (HD/VD) all decoupled as in ELISA. Furthermore the electrostatic deflection elements have cylindrical symmetry and are not doubly focusing.

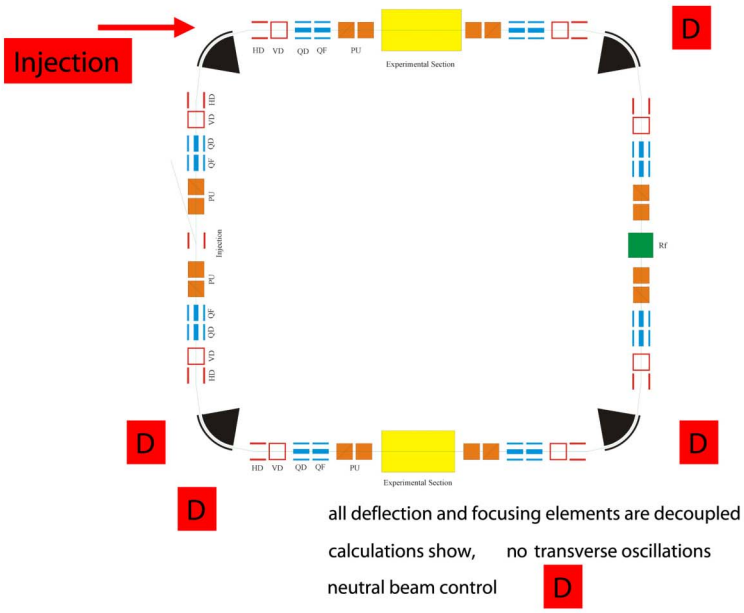

Figure 38: *A schematic drawing of the electrostatic storage ring for antiprotons.*

The length of each side is about 3 m. In two straight line sections space is reserved for experimental equipment like COLTRIMS, allowing investigations of complete momentum balances of many-particle reaction dynamics. The beam can be injected from various directions, (e.g. directly into the axis, or in the middle of a straight section). The microsec pulsed $\bar{p}$ beam from the ASACUSA RFQD could be directly injected, filling about 50% (depending on the beam energy) of the ring. Depending on the beam lifetime a luminescence amplification of about 10^5 for COLTRIMS coincidence studies could be achieved. This would enable even detailed studies of reaction dynamics with $\bar{p}$ beams.

The main scientific goals are the investigation of the many-particle dynamics using slow and fast $\bar{p}$ beams for comparison with results with protons and electrons. Thus the reaction microscope contains a well designed supersonic gas jet target. This requires special pumping of the ring, and four high-compression 500 l/sec Pfeiffer turbo pumps together with several getter pumps have been ordered to be able to pump He efficiently and achieve a ring pressure of 10^{-11} mbar. Tests of the pumping devices are now being performed. To monitor the ring beam performance at each end of all straight sections position-sensitive MCP detection devices (D) are implemented to monitor all beam scattering events. Since the ring will be used at Frankfurt and elsewhere mainly for beams (positive ions and positrons) which can capture electrons, the neutral beam components after capture can be detected. A 90° section with all focusing elements is presently being tested.

Since our proposal (for building the $\bar{p}$ ring) submitted to the German BMBF was not funded (no other proposal for research at the AD/CERN was funded by the BMBF either), we have decided to build the ring with money from other sources including industry. Thus we can order the pumping units, gauges, position-sensitive detectors, high voltage supplies etc., only in accordance with funding from these other sources. The construction will therefore take somewhat longer than originally scheduled in our BMBF proposal. We nevertheless expect that all necessary components can be acquired within the year 2002, and that the ring will be completed at the end of 2003.

The ring is being constructed by a collaboration of the groups of H.Schmidt-Böcking, A.Schempp and R.Dörner at the University Frankfurt (involved group members: C.Welsch, K.Stiebing, L.Schmidt, K.Schneider) in cooperation with S.Møller/Aarhus and the group of J.Ullrich/MPI-Heidelberg (reaction microscope).

9 Measurement of protonium and other X-ray spectra

9.1 A Possibility of Protonium X-ray Spectroscopy at the AD

This part was contributed by D. Gotta[2], H.J. Stein[1], H. Gorke[3] and K. Zwoll[2], who are not yet the members of ASACUSA collaboration. Physics possibilities using the quasi-continuous beam extracted from ASACUSA trap are being investigated in close collaboration, as shown below.

9.1.1 Motivation

A series of X-ray measurements on light antiprotonic atoms was performed during the LEAR era. Though considerable progress has been achieved in the understanding of the low-energy antinucleon-nucleon interaction the picture is far from being complete.

For protonium, the spin-averaged strong interaction shift and broadening of the atomic ground state were determined with an accuracy of the order of 10% (table 2), but no unambiguous determination of the hadronic effects for the individual hyperfine states could be obtained because of limited statistics and significant background (see Fig. 39). To improve, a high-statistics measurement of the protonium ground-state transition is needed (the goal is to collect 200,000 Lyman α events).

In antiprotonic deuterium, evidence was found for the ground-state transition. The observed small broadening is in line with an observation in low-energy $\bar{N}N$ scattering showing a decreasing annihilation strength with increasing atomic mass[61]. A confirmation of such a behaviour is urgently required (20,000 events).

Table 2: *Spin-averaged hadronic shifts ϵ and broadenings Γ in light antiprotonic atoms compared to theoretical predictions. The radiative decay widths of the 2p states in $\bar{p}H$ and $\bar{p}D$ are 0.38 meV and 0.51 meV.*

	ϵ_{1s} / eV	Γ_{1s} / eV		ϵ_{2p} / meV	Γ_{2p} / meV	
$\bar{p}H$						
experiment	-714 ± 14	1097 ± 42	[62]	$+15 \pm 20$	38.0 ± 2.8	[63]
DR1	-707	933	[64]	+6	33.5	[64]
KW	-698	1062	[64]	+7	35	[64]
eff.range	-600	1080	[65]	+9	39	[65]
$\bar{p}D$						
experiment	-1050 ± 250	1100 ± 750	[66]	-243 ± 26	489 ± 30	[63]
mult. scatt.	≈ -4000	≈ 5000	[67]	-52	422	[67]
3-body cal.	≈ -1600	≈ 1000	[68]			

[2] *Institut für Kernphysik, forschungszentrum Jülich, D-52425 Jülich, Germany*
[3] *Zentralabteilung für Elektronik, Forschungszentrum Jülich, D-52425 Jülich, Germany*

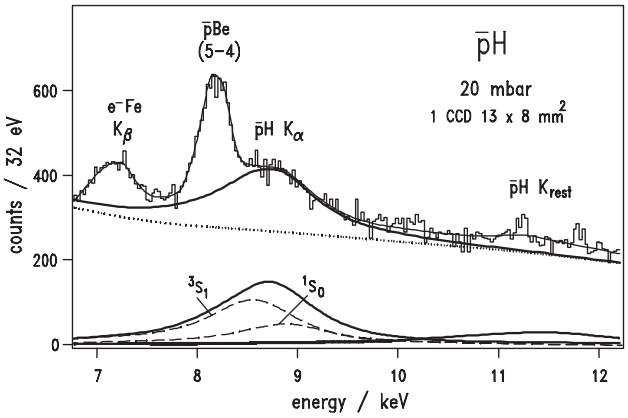

Figure 39: *X-ray spectrum in the energy range of the $\bar{p}H$ Lyman transitions measured with a CCD at LEAR (PS207 [62]). In total, about 20,000 events were attributed by the fit to the K_α transitions. Due to low statistics and significant background, unambiguous determination of the hadronic effects for the individual hyperfine states was not possible. A possibility to increase the statistics by a factor 10 using the quasi-continuous beam of ASACUSA is being investigated.*

9.1.2 A possible setup

The new Antiproton Decelerator AD at CERN provides only fast extraction of a few $10^7\bar{p}$ within ~ 300 ns. To use a significant fraction of these antiprotons for X-ray spectroscopy, quasi-continuous beam extracted from the ASACUSA trap, adapted to the read-out performance of CCDs, is needed.

Because of the low kinetic energy (< 1keV) at the exit of the extraction beam line following the trap, the antiprotons have to be reaccelerated to be able to penetrate a thin window of a low-pressure gas cell. The window is necessary to guarantee for the critical vacuum requirements of the catcher trap. Fig. 40 shows a scheme for such a reacceleration beam line.

The extension of the Bragg peak can be kept below 50 mm for a few mbar gas pressure. Energies of about 100 keV are sufficient to allow the use of a robust window and can still be operated by conventional high-voltage techniques. Fine tuning of the range may be feasible by adjusting the high voltage and the field of the magnetic lense.

When using hydrogen as target gas, impurities must be kept at the level of a few ppm in order to avoid significant capture in the higher Z atoms. Extraction from the catcher trap also offers the possibility to investigate antiprotonic X-rays emerging from any solid target especially if rare isotopes are used.

9.1.3 X-ray detector

A special type of Charge-Coupled Devices (CCDs) will become available (pn-CCDs), which can be read-out with modern data processing techniques in a few milliseconds. Such a CCD is ideally suited for the direct measurement of low yield Lyman transitions from protonium or the Balmer transitions from antiprotonic helium, but still requires to limit the antiproton flux to about 10^5 per second.

The solid angle achievable with pn-CCD of about 1 cm^2 area is of the order of 2 per mille. CCD efficiency is about 90% at energies around 10 keV, which is a factor of 3 higher than for the CCDs used in experiment PS207. The efficiency for the Balmer series (around 2 keV) will be more than 50% when using cryostats equipped with thin Be windows. Relative efficiency and energy

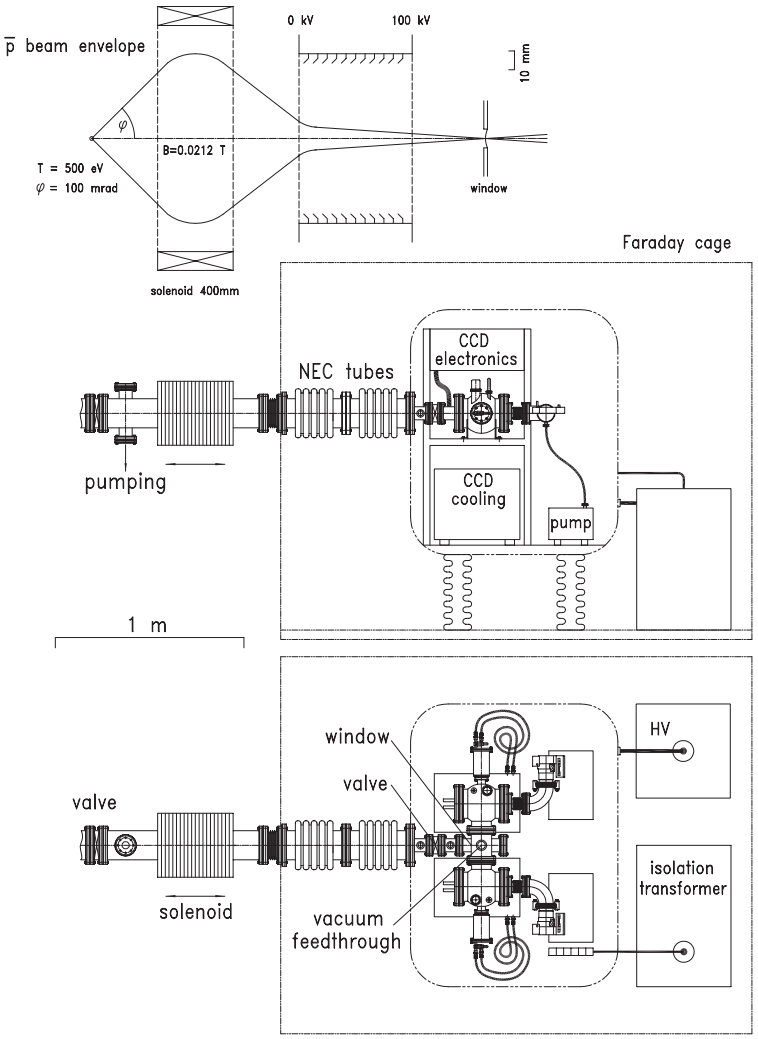

Figure 40: A schematic drawing of the reacceleration beam line to be attached to the extraction line downstream of the ASACUSA $\bar{p}$ trap. Gas cell and CCDs will be operated at high potential (up to 100 kV) so that quasi-continuous beam of antiprotons can penetrate the gas cell window.

resolution can be determined in-beam by the method of saturated lines from antiprotonic nitrogen, oxygen or neon.

9.1.4 Status and outlook

A design study of the reacceleration line is in progress at Jülich. NEC tubes able to provide in the acceleration voltage of up to 100 kV are available as a loan. Vacuum tubes, gas cell and support structures could be built in the workshop at FZJ and vacuum pumps are mostly available from other activities. The magnetic lens (coil), the high-voltage supply and the power transformer must be found or bought. The Faraday cage has to be built.

The high-rate capable CCDs are being set-up at the Central Electronics Laboratory (ZEL) and at the IKP of the FZ Jülich to be used among others for pionic X-ray measurements at PSI. They are part of another project and, therefore, are developed independently from a possible AD

experiment.

This experiment will become feasible when the tuning of the MUSASHI beam line is optimized, and $\sim 5 \times 10^6$ antiprotons / AD shot can be extracted. Line yield (1%) and solid angle (0.2% per CCD) of the X-ray detector result in approximately 10^{-5} K_α events per stopped antiproton or 40 events per AD shot and cm^2 CCD area. By using 2 CCDs, about 2500 shots will be necessary for the $\bar{p}H$ experiment, somewhat less for the $\bar{p}D$ experiment.

9.2 Antiprotonic X-rays from selected isotopically separated targets

This part was contributed by J. Jastrzębski[4], A. Trzcińska[3], S. Wycech[5], T. von Egidy[6] and B. Kłos[7], who are not yet the members of ASACUSA collaboration. Physics possibilities using the quasi-continuous beam extracted from ASACUSA trap are being investigated in close collaboration, as shown below.

9.2.1 Motivation

It is proposed to investigate the characteristics of antiprotonic X-rays in selected isotopically separated targets using ASACUSA setup. The first goal is to further study the neutron "halo" revealed in the PS209 experiment (see Fig. 41 [69], also see CERN Courier [70]). In addition, the present program seeks for more information useful in the construction of the antiproton-nucleon optical potential, presently under way.

To achieve these two goals we propose to search for odd-even effects in neutron distributions in Sn nuclei, to investigate simultaneously the properties of three antiprotonic levels in Ca nuclei, to study the abnormal upper level shifts and strong interaction effects on LS splitting in even deformed nuclei, to investigate the properties of hidden levels via E2 resonance and to search for bound $\bar{p}p$ state effects in X-ray spectra. In the following, the first two (Sn and Ca) are described in some detail. We expect that the completion of the proposed research program would practically exhaust the presently imaginable antiprotonic experiments studying the nuclear periphery in stable nuclei. It would also substantially increase the experimental basis for more adequate antiproton-nucleus optical potentials than presently available.

Although the PS209 experiment substantially increased the previously available level widths and shift data, there are still many interesting and open questions which could be investigated if new experiments could be performed. The answer to these questions would not only enlarge the amount of our information about the nuclear periphery but also contribute to the determination of a more elaborate antiproton-nucleon optical potential [71]. One expects that new potentials could help to explain a certain number of experimental data, difficult to understand with a simple, isoscalar antiproton-nucleon optical potential parameters available up to now. This is especially true for the observed level shifts, which are often underestimated by calculation based on these potentials.

9.2.2 Odd-even effects in the neutron distribution in nuclei

We have recently demonstrated[69] that the difference between rms neutron and proton radii, Δr_{np} is a linear function of the asymmetry parameter $\delta = (N - Z)/A$ (see Fig. 41). However, except for ^{57}Fe, all experimental data in this figure were gathered for even N nuclei. Using a radiochemical

[4] *Heavy Ion Laboratory, Warsaw University, PL-02-093, Warsaw, Poland*
[5] *Sołtan Institute for Nuclar Studies, PL-00-681, Warsaw, Poland*
[6] *Physik Department, Technische Universität München, D-85747 Garching, Germany*
[7] *Silesian University, PL-40-007, Katowice, Poland*

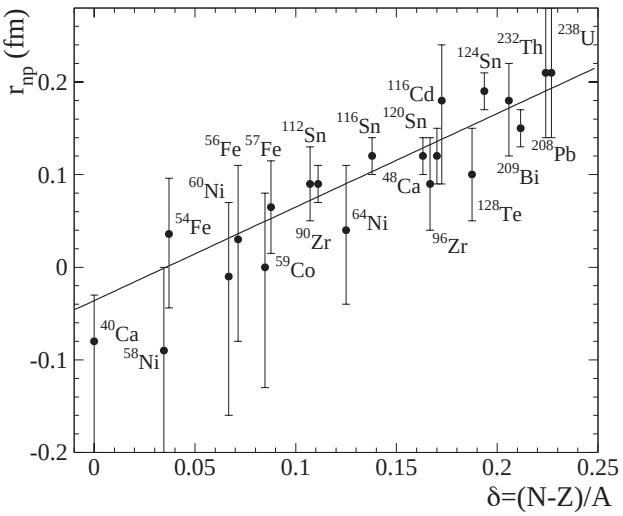

Figure 41: *Difference Δr_{np} between the rms radii of the neutron and proton distributions as deduced from the antiprotonic X-ray data, as a function of $\delta = (N - Z)/A$.*

method, PS203 also showed that at least for even-A nuclei the neutron peripheral distribution is strongly negatively correlated with target neutron separation energy.

The open question is if the difference between neutron separation energy in even-N and odd-N nuclei of the same element has a noticeable influence on the Δr_{np} values of these nuclei. This question could not be answered using the radiochemical experiment as there are no odd-N targets with both $A_t - 1$ products being radioactive. The beam time limitation of the PS209 experiment was the reason why this question was not fully answered by experiments in 1995 and 1996. As yet there are no theoretical HFB estimations of the odd-even effect influence on Δr_{np} values.

As the first search for this effect we propose the studies of the level widths and shifts in ^{117}Sn, ^{118}Sn, ^{119}Sn and ^{120}Sn. The ^{120}Sn target was already investigated within PS209 experiment and will constitute a reference point for a new series of experiments.

9.2.3 Detailed study of Ca antiprotonic atoms

Within the PS209 experiment we have investigated the X-ray spectra of ^{40}Ca, ^{42}Ca, ^{43}Ca, ^{44}Ca and ^{48}Ca [34]. Also, ^{48}Ca was studied using the radiochemical method and its "halo factor" was determined. These data are of special interest for nuclear periphery studies since they include the doubly magic ^{40}Ca and ^{48}Ca nuclei. The nuclear structure of these nuclei was investigated theoretically as well as experimentally for decades. Therefore, to a large extent, they may be considered as a test case for any new method used for nuclear periphery investigation. Also, in Ca nuclei there is an almost unique possibility of a simultaneous determination of 3 level widths and 2 level shifts, providing a very weak (about 2% relative intensity) $n = 5 \rightarrow n = 4$ transition is measured. Such an information would be of a great help in antiproton-nucleus optical potential parameterization.

The $5 \rightarrow 4$ transition was previously observed in ^{40}Ca in PS176 experiment in 1985 where a metallic target was employed. In our PS209 investigation we only disposed of targets in form of $CaCO_3$ pellets placed within mylar bags. This target composition resulted in a rather high background making the observation of this transition difficult.

We hence propose to determine the properties of this level for individual Ca isotopes using thin metallic targets.

Moreover, the study of the very expensive ^{43}Ca isotope could be possible using a very thin target in this ASACUSA setup. The PS209 data for this isotope were gathered with a target of only 31% A=43 abundance. The odd-even effect, described in the previous section, seems to show up at least for the $n = 5$ level shift, but the low ^{43}Ca abundance in the target makes this result uncertain.

9.2.4 Status and outlook

The experimental setup will be positioned at the end of the ASACUSA $\bar{\text{p}}$ trap and is rather simple. Isotope-enriched thin metallic target is mounted inside the vacuum, and X-rays are detected by using high-resolution Ge detectors. Pions emitted from $\bar{\text{p}}$ annihilation are detected to provide event trigger.

In the first stage of the experiment, the X-ray detectors and associated electronics available at Heavy Ion Laboratory will be used. These are two ORTEC coaxial detectors of relative efficiencies of 17% and 19% and one planar detector (13 mm $\times$ 490 mm^3). One of the coaxial detectors can be placed in an available BGO shield to suppress the Compton background. In the second stage, we can try to use simultaneously a larger number of HPGe detectors.

With the trigger efficiency of $\eta_{\text{pion}} \approx 70\%$, the efficiency of the Ge counters for X-ray detection $\eta_{\text{X}} \approx 5 \cdot 10^{-4}$, the $5 \rightarrow 4$ x-ray yield per stopped $\bar{\text{p}}$ of $p_X \approx 2\%$ (in the case of Ca, which is the most difficult case) and an enrichment of $c_{\text{isotope}} = 80\%$, the overall efficiency is $\eta = \eta_{\text{pion}} \cdot \eta_{\text{X}} \cdot p_{\text{X}} \cdot c_{\text{isotope}} = 5 \cdot 10^{-6}$. *If 10^6 antiprotons can be extracted from the trap per AD shot, 3600 counts in this Ca $5 \rightarrow 4$ line can be accumulated in three 8-hour shifts.*

References

[1] ASACUSA collaboration, Atomic spectroscopy and collisions using slow antiprotons, Proposal CERN/SPSC 97-19, 1997.

[2] M. Hori, J. Eades, E. Widmann, H. Yamaguchi, J. Sakaguchi, T. Ishikawa, R. S. Hayano, H. A. Torii, B. Juhász, D. Horváth, and T. Yamazaki, Phys. Rev. Lett. 87 (2001) 093401.

[3] S.P.Møller, A. Csete, T. Ichioka, H. Knudsen, U. Uggerhøj, and H. Andersen, submitted to Physical Reveiw letters nov 2001 .

[4] ASACUSA collaboration, Status report, CERN/SPSC 2001-006, 2001.

[5] D. Bakalov and V. I. Korobov, Phys. Rev. A 57 (1998) 1662.

[6] V. Korobov and D. Bakalov, J. Phys. B: At. Mol. Opt. Phys. 34 (2001) L519.

[7] N. Yamanaka, Y. Kino, H. Kudo, and M. Kamimura, Phys. Rev. A 61 (2000) 012518.

[8] Y. Kino, N. Yamanaka, M. Kamimura, and H. Kudo, High precision calculation of the fine and hyperfine structure of antiprotonic helium-3,4 atoms, in *Proceedings of the 3rd European Conference on Atomic Physics at Accelerators (APAC2001)*, Aarhus, Denmark, 2001, Hyperfine Interactions, in press.

[9] G. Ya. Korenman, in *Abstract Book of the Asia-Pacific Few Body Conference (APFB99)*, Kashiwa, 1999.

[10] Y. Kino, private communication, 2001.

[11] D. Bakalov, Nucl. Phys. A 655 (1999) 301c.

[12] D. Groom et al., The European Physical Journal C 15 (2000) 1.

[13] V. I. Korobov, Nucl. Phys. A 689 (2001) 75c.

[14] Y. Kino, M. Kamimura, and H. Kudo, Hyperfine Intractions 119 (1999) 201.

[15] H. A. Torii, R. S. Hayano, M. Hori, T. Ishikawa, N. Morita, M. Kumakura, I. Sugai, T. Yamazaki, B. Ketzer, F. J. Hartmann, T. von Egidy, R. Pohl, C. Maierl, D. Horváth, J. Eades, and E. Widmann, Phys. Rev. A 59 (1999) 223.

[16] P. Robertson, T. King, R. Kunselman, J. Miller, R. J. Powers, P. D. Barnes, R. A. Einstein, R. B. Sutton, W. C. Lam, C. R. Cox, M. Eckhause, J. R. Kane, A. M. Rushton, W. F. Vulcan, and R. E. Welsh, Phys. Rev. C 16 (1977) 1945.

[17] T. Yamazaki and K. Ohtsuki, Phys. Rev. A 45 (1992) 7782.

[18] V. I. Korobov and I. Shimamura, Phys. Rev. A 56 (1997) 4587.

[19] O. Kartavtsev, D. Monakhov, and S. Fedotov, Phys. Rev. A 61 (2000) 062507, Errata 61 (2000) 019901(E).

[20] V. I. Korobov, private communication, 2000.

[21] G. Ya. Korenman, Hyperfine Interact. 101/102 (1996) 81.

[22] W. A. Beck, L. Wilets, and M. A. Alberg, Phys. Rev. A 48 (1993) 2779.

[23] J. S. Cohen, Phys. Rev. A 62 (2000) 022512.

[24] S. Sauge and P. Valiron, Chem. Phys. 265 (2001) 47.

[25] M. Hori, J. Eades, E. Widmann, H. Yamaguchi, J. Sakaguchi, T. Ishikawa, R. S. Hayano, H. A. Torii, B. Juhász, D. Horváth, and T. Yamazaki, submitted to Phys. Rev. Lett.

[26] Y. Yamazaki, in *Proceedings of Non-Neutral Plasma Physics III, Princeton, New Jersey 2001*, edited by J. Bollinger, R. Spencer, and R. Davidson, American Institute of Physics, New York, 1999,, p. 48.

[27] H.Higaki and A.Mohri, J.J.Appl.Phys. 36 (1997) 5300.

[28] A.Mohri, H.Higaki, H.Tanaka, Y.Yamazawa, M.Aoyagi, T.Yuyama, and T.Michishita, J.J.Appl.Phys. 37 (1998) 664.

[29] K. Franzen, H.Higaki, T.Ichioka, M.Hori, Z.Wang, N.Kuroda, S.Yoneda, H.A.Torii, K.Komaki, and Y.Yamazaki, in *Proceedings of the International Workshop on Nonneutral Plasmas 2001*, (to be published).

[30] S. P. Møller, E. Uggerhøj, H. Bluhme, H. Knudsen, U. Mikkelsen, K. Paludan, and E. Morenzoni, Phys. Rev. A 56 (1997) 2930.

[31] See *e.g.*: H. H. Mikkelsen, Nucl. Instrum. Methods Phys. Res., Sect. B 58 (1991) 136.

[32] See *e.g.*: P. Sigmund and A. Schinner, submitted to 19'th International Conference on Atomic collisions in solids, Paris, 2001, to be published in Nucl. Instr. Methods B; P. Sigmund and A. Schinner, Eur. Phys. J. D15 (2001) 165.

[33] H. Andersen, A. Csete, T. Ichioka, H. Knudsen, S. Møller, and U. Uggerhøj, Submitted to Nuclear Instruments and Methods B (2001).

[34] ICRU report 49, Stopping Powers and Ranges for Proton and Alpa Particles, 0-913394-47-5 (1993).

[35] Y.-N. Wang and T.-C. Ma, Nucl. Instrum. Methods Phys. Res., Sect. B 51 (1990) 16.

[36] B. Ketzer, F. J. Hartmann, T. von Egidy, C. Maierl, R. Pohl, J. Eades, E. Widmann, T. Yamazaki, M. Kumakura, N. Morita, R. S. Hayano, M. Hori, T. Ishikawa, H. A. Torii, I. Sugai, and D. Horváth, Phys. Rev. Lett. 78 (1997) 1671.

[37] B. Ketzer, F. J. Hartmann, T. von Egidy, C. Maierl, R. Pohl, J. Eades, E. Widmann, T. Yamazaki, M. Kumakura, N. Morita, R. S. Hayano, M. Hori, T. Ishikawa, H. A. Torii, I. Sugai, and D. Horváth, J. Chem. Phys. 109 (1998) 424.

[38] B. Ketzer, T. von Egidy, F. J. Hartmann, C. Maierl, R. Pohl, J. Eades, E. Widmann, T. Yamazaki, M. Kumakura, N. Morita, R. S. Hayano, M. Hori, T. Ishikawa, H. A. Torii, I. Sugai, and D. Horváth, Europ. Phys. J. D 13 (2001) 305.

[39] B. Juhász, J. Eades, R. S. Hayano, M. Hori, D. Horváth, T. I. shikawa, J. Sakaguchi, H. A. Torii, E.Widmann, H. Yamaguchi, and T. Yamazaki, Eur. J. Phys. D (2001), in press.

[40] S. Sauge and P. Valiron, submitted to Chem. Phys. (2001).

[41] H. Knudsen, U. Mikkelsen, K. Paludan, K. Kirsebom, S. Møller, E. Uggerhøj, J. Slevin, M.Charlton, and E. Morenzoni, Phys. Rev. Lett. 74 (1995) 4627.

[42] P. Hvelplund, H. Knudsen, U. Mikkelsen, E. Morenzoni, S. Møller, E. Uggerhøj, and T.Worm, Journal of Physics B 27 (1994) 925.

[43] G. O. Jones, M. Charlton, J. Slevin, G. Laricchia, A. Köver, M. Poulsen, and S. N. Chormaic, Journal of Physics B 26 (1993) L483.

[44] G. O. Jones, Ph D Thesis, University College London (1993) (unpublished).

[45] Y. Yamazaki, in *Proceedings of Non-Neutral Plasma Physics III, Princeton, New Jersey 2001*, edited by J. Bollinger, R. Spencer, and R. Davidson, American Institute of Physics, New York, 1999,, p. 48.

[46] E. Fermi and E. Teller, Phys. Rev. 72 (1947) 399.

[47] J. Cohen, Phys. Rev. A 56 (1997) 3583.

[48] R. Moshammer, J. Ullrich, M. Unverzagt, W. Schmidt, P. Jardin, R. Olson, R. Mann, R. Dörner, V. Mergel, U. Buck, and H. Schmidt-Böcking, Phys. Rev. Lett. 73 (1994) 3371.

[49] R. Moshammer, P. Fainstein, M. Schulz, W. Schmitt, H. Kollmus, R. Mann, S. Hagmann, and J. Ullrich, Phys. Rev. Lett. 83 (1999) 4721.

[50] M. Schulz, R. Moshammer, D. Madison, R. Olson, P. Marchalant, C. Whelan, H. Walters, S. Jones, M. Foster, H. Kollmus, A. Cassimi, and J. Ullrich, J. Phys. B 34 (2001) L305.

[51] R. Moshammer, A. Perumal, M. Schulz, H. Kollmus, R. Mann, S. Hagmann, and J. Ullrich, Phys. Rev. Lett. (2001), (accepted).

[52] M. Schulz, R. Moshammer, A. Perumal, and J. Ullrich, Phys. Rev. Lett. (2001), (submitted).

[53] V. Mergel, R. Dörner, M. Achler, K. Khayyat, S. Lencinas, J. Euler, O. Jagutzki, S. Nüttgens, M. Unverzagt, L. Spielberger, W. Wu, R. Ali, J. Ullrich, H. Cederquist, A. Salin, R. Olson, D. Belkić, C. Cocke, and H. Schmidt-Böcking, Phys. Rev. Lett. 79 (1997) 387.

[54] R. Moshammer, M. Unverzagt, W. Schmitt, J. Ullrich, and H. Schmidt-Böcking, Nucl. Instrum. Methods Phys. Res., Sect. B 108 (1996) 425.

[55] R. Dörner, V. Mergel, O. Jagutzki, L. Spielberger, J. Ullrich, R. Moshammer, and H. Schmidt-Böcking, Phys. Rep. 330 (2000) 96.

[56] K. Khayyat, T. Weber, R. Dörner, M. Achler, V. Mergel, L. Spielberger, O. Jagutzki, U. Meyer, J. Ullrich, R. Moshammer, W. Schmitt, H. Knudsen, U. Mikkelsen, P. Aggerholm, E. Uggerhoej, S. Møller, V. Rodríguez, S. O'Rourke, R. Olson, J. McGuire, and H. Schmidt-Böcking, J. Phys. B 32 (1999) L73.

[57] D. Schultz, P. Kristić, C. Reinhold, and J. Wells, Phys. Rev. Lett. 76 (1996) 2882.

[58] R. Dörner, H. Khemliche, M. Prior, C. Cocke, J. Gary, R. Olson, V. Mergel, J. Ullrich, and H. Schmidt-Böcking, Phys. Rev. Lett. 77 (1996) 4520.

[59] GSI-KKS, Förderkennzeichen 06HD994.

[60] S.P.Møller, Nucl. Instrum. Methods Phys. Res., Sect. A 394 (1997) 281.

[61] K. Protasov, G. Bonomi, E. Lodi-Rizzini, and A. Zenoni, Eur. Phys. J. A 7 (2000) 429.

[62] M. Augsburger, D. Anagnostopoulos, G. Borchert, D. Chatellard, J.-P. Egger, H. Gorke, D. Gotta, P. Hauser, P. Indelicato, P. El-Khoury, K. Kirch, S. Lenz, K. Rashid, T. Siems, and L. Simons, Nucl. Phys. A 658 (1999) 149.

[63] D. Gotta, D. Anagostopoulous, M. Augsburger, G. Borchert, C. Castelli, D. Chatellard, J.-P. Egger, P. El-Khoury, H. Gorke, P. Hauser, P. Indelicato, K. Kirch, S. Lenz, N. Nelms, K. Rashid, T. Siems, and L. Simons, Nucl. Phys. A 660 (1999) 283.

[64] J. Carbonell, G. Ihle, and J. Richard, Z. Phys. A 334 (1989) 329.

[65] I. Grach, B. Kerbikov, and Y. Simonov, Sov. J. Nucl. Phys. A 48 (1988) 609.

[66] M. Augsburger, D. Anagnostopoulous, G. Bochert, D. Chatellard, J.-P. Egger, H. Gorke, D. Gotta, P. Hauser, P. Indelicato, P. El-Khoury, K. Kirch, S. Lenz, K. Rashid, T. Siems, and L. Simons, Phys. Lett. B 461 (1999) 417.

[67] S. Wycech, A. Green, and J. A. Niskanen, Phys. Lett. 152 B (1985) 308.

[68] G. Latta and P. Tandy, Phys. Rev. C 42 (1990) R1207.

[69] A. Trzcińska, J. Jastrzębski, P. Lubiński, F. Hartmann, R. Schmidt, T. von Egidy, and B. Kłos, Phys. Rev. Lett. 87 (2001) 082501.

[70] Cern Courier November 2001 20.

[71] S. Wycech, Nucl. Phys. A 692 (2001) 29c.